

Shallow shell theory of the buckling energy barrier: From the Pogorelov state to softening and imperfection sensitivity close to the buckling pressure

Lorenz Baumgarten^{1,2,*} and Jan Kierfeld^{2,†}

¹*Institute for Theoretical Physics, University of Bremen, 28359 Bremen, Germany*

²*Physics Department, TU Dortmund University, 44221 Dortmund, Germany*

(Dated: February 26, 2019)

We study the axisymmetric response of a complete spherical shell under homogeneous compressive pressure p to an additional point force. For a pressure p below the classical critical buckling pressure p_c , indentation by a point force does not lead to spontaneous buckling but an energy barrier has to be overcome. The states at the maximum of the energy barrier represent a subcritical branch of unstable stationary points, which are the transition states to a snap-through buckled state. Starting from nonlinear shallow shell theory we obtain a closed analytical expression for the energy barrier height, which facilitates its effective numerical evaluation as a function of pressure by continuation techniques. We find a clear crossover between two regimes: For $p/p_c \ll 1$ the post-buckling barrier state is a mirror-inverted Pogorelov dimple, and for $(1 - p/p_c) \ll 1$ the barrier state is a shallow dimple with indentations smaller than shell thickness and exhibits extended oscillations, which are well described by linear response. We find systematic expansions of the nonlinear shallow shell equations about the Pogorelov mirror-inverted dimple for $p/p_c \ll 1$ and the linear response state for $(1 - p/p_c) \ll 1$, which enable us to derive asymptotic analytical results for the energy barrier landscape in both regimes. Upon approaching the buckling bifurcation at p_c from below, we find a softening of an ideal spherical shell. The stiffness for the linear response to point forces vanishes $\propto (1 - p/p_c)^{1/2}$; the buckling energy barrier vanishes $\propto (1 - p/p_c)^{3/2}$; and the shell indentation in the barrier state vanishes $\propto (1 - p/p_c)^{1/2}$. This makes shells sensitive to imperfections which can strongly reduce p_c in an avoided buckling bifurcation. We find the same softening scaling in the vicinity of the reduced critical buckling pressure also in the presence of imperfections. We can also show that the effect of axisymmetric imperfections on the buckling instability is identical to the effect of a point force that is preindenting the shell. In the Pogorelov limit, the energy barrier maximum diverges $\propto (p/p_c)^{-3}$ and the corresponding indentation diverges $\propto (p/p_c)^{-2}$. Numerical prefactors for proportionalities both in the softening and the Pogorelov regime are calculated analytically. This also enables us to obtain results for the critical unbuckling pressure and the Maxwell pressure.

I. INTRODUCTION

When a complete spherical elastic shell is put under homogeneous mechanical compressive pressure, the spherical shape remains stable over a considerable pressure range until it finally collapses at the critical buckling pressure p_c . This pressure has been known for over one hundred years since the work of Zoelly [1] and buckling is an ubiquitous mode of failure for curved thin-walled shells with significant implications for all engineering applications [2]. Buckling represents a hysteretic bifurcation analogously to a hysteretic first-order transition in a thermodynamic system because the buckled state is already metastable below p_c [3]. Therefore, the shell can be “pushed” into a buckled state containing a single axisymmetric dimple already below p_c by applying an additional localized point force. A threshold force is required to create a stable dimple, and the required threshold value increases for decreasing p further below p_c . This corresponds to an energy barrier that has to be overcome by applying the additional point force before the spherical shell buckles. This energy barrier has been

subject of a number of recent studies both for spherical [4–10] and cylindrical [8, 10, 11] shells. Obviously, it is an important feature that governs the mechanical stability of spherical shell structures slightly below the buckling threshold with respect to localized point forces, but also with respect to thermal fluctuations [9, 12]. It also plays a prominent role for the buckling behavior of a shell containing inhomogeneities or imperfections in the form of “frozen-in” normal displacements in the rest state of the shell [13–15] or soft spots [16]; both are problems that we will also revisit. The energy barrier represents also an important feature of a spherical shell from a general theoretical point of view as the barrier vanishes upon approaching the buckling bifurcation and how it vanishes characterizes the critical behavior of the buckling bifurcation. In the mechanics literature, the unstable barrier state is often referred to as post-buckling state [14] as the shell already contains a dimple; the catastrophic nature of the buckling instability is reflected in a decreasing pressure $p < p_c$ of the barrier state, which leads to a snap-through buckling [3, 17]. Many quantitative analytical results on buckling of spherical shells are based on the Pogorelov theory, where the dimple is approximated as a mirror-inverted spherical cap-shaped indentation [18]. Here, we present a rigorous quantitative approach on the energy barrier based on systematic expansions of nonlinear shallow shell theory. Expanding about the Pogorelov

* lbaumgarten@itp.uni-bremen.de

† jan.kierfeld@tu-dortmund.de

mirror-inverted dimple we find analytical results for the energy barrier in the Pogorelov limit $p/p_c \ll 1$. This extends recent work of Gomez *et al.* on the Pogorelov indentation in the absence of pressure [19] and is conceptually similar to the boundary layer approach of Evkin *et al.* [5, 20, 21]. We also derive analytical results for the “critical” regime of pressures close to p_c by an expansion about the linear response state for $(1 - p/p_c) \ll 1$. This enables us to characterize the softening of the capsule close to the critical pressure.

Elastic shells are thin-walled elastic structures with a curved reference shape. Bending energy penalizes deviations in curvature from the spontaneous curvature of the reference shape, and two-dimensional elastic energy penalizes stretching and shear deformations of the quasi-two-dimensional shell with respect to the reference shape, in which the capsule is stress free. Examples for elastic shells range from the micro- to the macroscale. On the microscale, artificial microcapsules enclosing a liquid [22–25] can be described as elastic shells. On the macroscale, all thin-walled spherical structures in mechanical engineering (vessels, domelike structures, egg shells [26]) provide examples. Red blood cells [27–30] and shells of viruses [31, 32] have elastic properties similar to continuum elastic shells but there are important differences, for example, regarding the reference shape and crystallinity. Here, we consider elastic shells with a spherical reference shape with radius R_0 . For red blood cells, the rest shape is, however, not spherical but an oblate spheroid [29, 30]. Because a sphere has minimal area for a given volume, any deformation of the spherical rest shape involves stretching, whereas red blood cells are known to undergo shape transformations at (even locally) conserved area [27–30]. Viruses are crystalline spherical shells consisting of discrete protein building blocks. Any triangulation of a sphere must contain at least 12 fivefold disclinations. Continuum shell theory cannot account for such defects, which give rise to faceted equilibrium shapes of large viruses, while sufficiently small viruses remain spherical [31]. The faceted equilibrium shape of large viruses is an important difference to spherical shells. In contrast to quasi-two-dimensional elastic shells, vesicles are quasi-two-dimensional fluid membranes made from lipid bilayers. Vesicles also have a bending and stretching energy but lack a shear energy because of their fluidity. They show a distinct deformation behavior as compared to elastic capsules [33]. In particular, their response to additional point forces is different because of the lack of an elastic reference state. For vesicles, additional point forces lead to tube formation [34, 35] rather than the formation of a dimple; such tubes can also be stabilized by actin protrusions [36]. Only in its gel phase can a vesicle acquire a shear modulus and exhibit elastic features similar to an elastic shell. Also, biological cells have an elastic cortex which can be modeled as an elastic shell if it is sufficiently thin [37]. If the cortex spans the entire cell, the cell should be treated as a solid elastic sphere [37, 38]. Moreover, active motor-induced stresses can modify the

actin cortex elasticity [39].

If the capsule material can be viewed as a thin shell of thickness h ($\ll R_0$) made from an isotropic and homogeneous elastic material with bulk Young’s modulus E , the shell has a bending modulus $\kappa \propto Eh^3$ but a two-dimensional Young’s modulus $Y \propto Eh$ [40, 41]. Therefore, bending deformations are energetically preferred over stretching or shear deformations for thin shells, as long as $R_0 \gg (\kappa/Y)^{1/2} \propto h$. As a result, spherical elastic shells or capsules are very resistant to compressive forces because there are no isometric, stretch- and shear-avoiding deformations of a sphere. Only above the critical pressure p_c does a perfect spherical shell become unstable and buckling occurs [40, 42].

At p_c , the buckling instability is triggered by a short-wavelength mode, which spreads over the whole sphere and leads to many small-amplitude dimples appearing on the sphere, as can be found in a linear stability analysis [13, 14, 16]. After this mode has developed, the shell can further lower its energy by increasing the amplitude, and nonlinearities in the elastic theory finally lead to coalescence of small dimples into a single dimple in the buckled energy minimum [9]. Following Pogorelov [18], the final dimple can be viewed as an approximative inverted spherical cap whose sharp edge at the rim is rounded to avoid infinite bending energies. Such a rounded spherical cap is an approximative isometry of the spherical rest shape. For a fixed mechanical pressure $p \geq p_c$, the dimple will actually snap through and grow until opposite sides are in contact, whereas for osmotic pressure control or even volume control, a stable dimple shape is reached before opposite sides come into contact [3, 17]. A deep dimple can also assume a polygonal shape in a *secondary* buckling transition [43–45].

Understanding the critical properties of the buckling instability is important both from a structural mechanics perspective for macroscopic spherical shells and for many applications of spherical microcapsules. For ideal spherical shells the classical buckling pressure p_c is known exactly. For a shell with rest radius R_0 , bending rigidity κ , two-dimensional (2D) Young’s modulus Y , one finds [1, 42, 46]

$$p_c = 4 \frac{\sqrt{Y\kappa}}{R_0^2} = 4 \frac{Eh^2}{R_0^2 \sqrt{12(1-\nu^2)}} = 4 \frac{Y}{R_0} \gamma^{-1/2}. \quad (1)$$

The second equality applies for thin shells of thickness h made from an isotropic elastic material with bulk Young modulus E and Poisson ratio ν , where $\kappa = Eh^3/12(1 - \nu^2)$ and $Y = Eh$ [46]. We also introduced the Föppl-von Kármán number

$$\gamma \equiv \frac{Y R_0^2}{\kappa} = 12(1 - \nu^2) \left(\frac{R_0}{h} \right)^2, \quad (2)$$

which is an inverse dimensionless bending rigidity. The ideal critical pressure p_c is, however, not reached in experiments on macroscopic shells, because imperfections reduce the buckling pressure significantly [13, 14].

Buckling represents a hysteretic bifurcation analogous to a hysteretic first order transition in a thermodynamic system; metastable buckled states and a corresponding unstable transition state appear already subcritically for $p < p_c$ [3, 5, 7, 9, 17]. The buckled state with a single axisymmetric dimple becomes *energetically* favorable already for $p > p_{c1}$, above the so-called *Maxwell pressure*, which can be obtained from a Maxwell construction of equal energies [3, 5, 7, 17] resulting in a parameter dependence $p_{c1} \sim p_c \gamma^{-1/4}$ [17]. As a result, there is a rather wide pressure window $p_c > p > p_{c1}$, where buckling is energetically possible but an energy barrier has to be overcome; the barrier state is an unstable transition state. One way to probe the energy barrier is by application of an additional point force, which “pushes” the shell into the buckled state [4–8, 10], see Fig. 1. If the dimple is created by a point force it is axisymmetric about the force axis. We exclusively study the axisymmetric situation in this paper. SURFACE EVOLVER simulations have shown, however, that the axisymmetric dimple is also the relevant barrier state if the dimple is not forced into an axisymmetric shape by a point force [9].

Below the Maxwell pressure, there is also a critical *unbuckling pressure* $p_{cu} \sim 3p_{c1}/4$, below which no stable buckled shape exists and which has the same parameter dependence as p_{c1} [3, 5, 16, 47]. This pressure is also called *minimum buckling load* in the literature [14, 48]. This gives the following general bifurcation scenario: Buckled states and the unstable barrier transition state appear in a bifurcation at $p = p_{cu}$. In the range $p_{cu} < p < p_c$, three stationary shapes are present: Spherical and buckled states are (meta)stable and separated by the unstable barrier state. At $p = p_c$, the barrier state and the spherical state vanish in a second bifurcation.

Whereas the value of the critical buckling pressure p_c is known analytically, many aspects of the buckling bifurcation are unexplored, in particular with respect to the buckling energy barrier. One example is the properties of the subcritical axisymmetric barrier state for p close to p_c . They characterize the bifurcation at p_c but have, so far, not been explored systematically. A systematic numerical and analytical investigation in this regime is the focus of the present paper. Most of the known results for the barrier state and the energy barrier height have been derived in the limit $p \ll p_c$ either from numerical work starting from energy minimization [6, 7, 9] or based on the Pogorelov energy scaling of the buckled state, which is only valid for relatively deep mirror-buckled indentations at $p \ll p_c$. The scaling of the energy barrier height $E_B \propto (p/p_c)^{-3}$ and the depth of the barrier indentation $z_B \propto (p/p_c)^{-2}$ can be derived using this Pogorelov scaling [9, 16, 17]. In the Pogorelov approach, numerical prefactors in the scaling results can be obtained from only an approximative variational energy minimization for the rounding of the sharp edge of inverted spherical cap shapes. Further progress has been made by Evkin and coworkers using a more systematic boundary layer formulation in shallow shell theory but still relying on

variational energy minimization [5, 20, 21].

In this paper, we start from the force equilibrium for axisymmetric states and use the nonlinear shallow shell equations to systematically derive properties of the buckling energy barrier. First, we will present numerical results based on an exact and explicit expression for the energy barrier in axisymmetric nonlinear shallow shell theory. Then we will focus both on the Pogorelov limit $p \ll p_c$, where we systematically expand about a mirror-symmetric barrier state with a deep indentation, and on the limit of compressive pressures below but close to p_c , where the barrier state is a very shallow dimple such that we can systematically expand about Reissner solutions of the linearized shallow shell theory. In both limits, we derive the exact asymptotic behavior including numerical prefactors. This enables us to obtain a complete picture of the buckling energy landscape in both limits and shed light on the critical properties of the buckling bifurcation.

In numerical calculations, application of a point force allows us to slowly push the shell into a buckled state, to explore thereby the buckling energy landscape, to detect the barrier state as the unstable force-free transition state, and to quantify the energy of the barrier state by measuring the work performed by the point force until the barrier is reached. Point forces are, however, also an important experimental tool to test shells [4]. Of particular interest in applications is the initial linear response of a shell to point forces because many mechanical compression techniques (plate compression [49, 50] or compression by microscopy tips [50, 51]) are equivalent to point force indentation in the initial small displacement regime. We provide an expression for the linear stiffness of the elastic shell, which is valid for the entire pressure range and extends results for pressurized capsules with stretching pressures [52] to compressive pressures up to the critical buckling pressure. Knowledge of the linearized stiffness can be used for measuring elastic capsule properties and capsule pressure [52].

Within the same framework of nonlinear shallow shell equations, we finally consider the effect of axisymmetric imperfections within the systematic expansion for shallow indentations. This allows us to explore how softening of the shell close to p_c makes shells sensitive to imperfections and results in an avoided buckling bifurcation. We compare the effect of a point force that is preindenting the shell with the effects of axisymmetric imperfections on the buckling instability and find striking similarities.

II. NONLINEAR SHALLOW SHELL THEORY

We employ nonlinear shallow shell theory for a thin spherical shell with equilibrium radius R_0 [41, 46], which is subject to a homogeneous compressive pressure p and an additional indenting point force F normal to the surface (see Fig. 1). We focus on isotropic elastic materials; isotropic Hookean elasticity can describe the deformation behavior of most artificial microcapsules rather well [53].

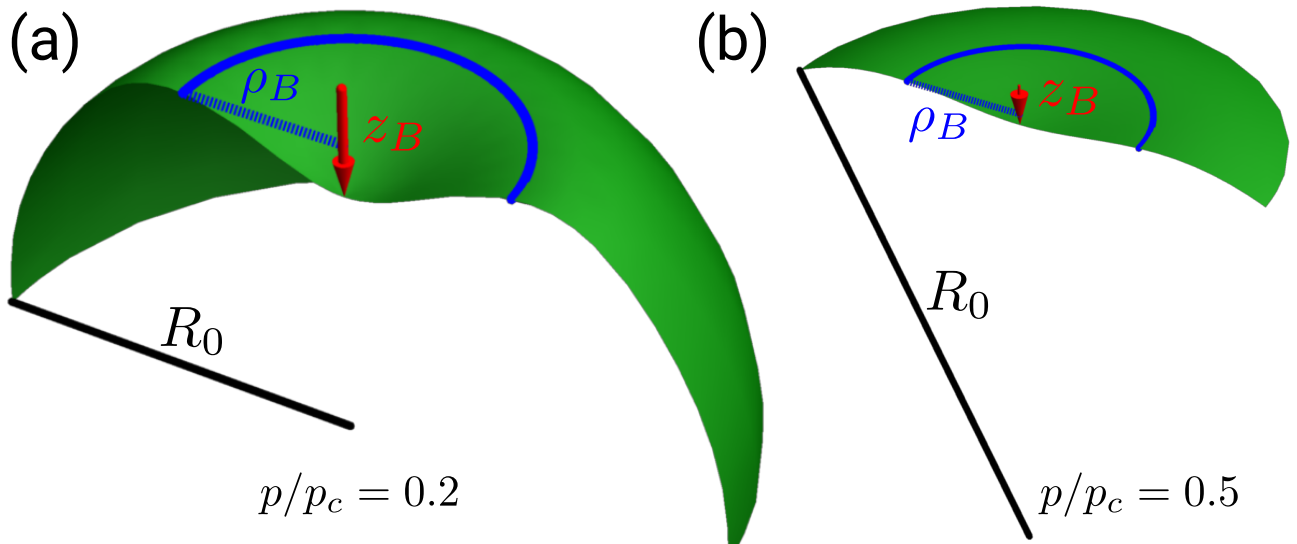


FIG. 1. Numerical results for the shape of a buckled spherical shell with $\gamma = 5000$ and rest radius R_0 in the postbuckling barrier state for pressures $p/p_c = 0.2$ (a) and $p/p_c = 0.5$ (b) according to nonlinear shallow shell equations (only the relevant part of the sphere is shown). The red arrow indicates the normal displacement z_B at the pole, which is also the direction of the applied point force. The blue ring indicates the width ρ_B of the barrier state.

Using polar coordinates r and ϕ on the two-dimensional reference plane over which shallow shell configurations are parametrized with the point force acting at the pole, shallow shell theory gives two coupled equations for the normal displacement $w(r, \phi)$ (negative for inward displacement) and the Airy stress function $\Phi(r, \phi)$. For axisymmetric states, as they are enforced by the point force, these functions become independent of ϕ , and we have two equations for $w(r)$ and the negative derivative of the Airy stress function $\psi(r) = -\Phi'(r)$, which have been derived and are described in detail in the literature [13, 16, 19, 46, 52] [see also Eqs. (87) and (88) in Appendix B with $w_I = 0$],

$$\kappa \nabla^4 w + \frac{1}{R_0} \frac{1}{r} \partial_r (r \psi) - \frac{1}{r} \partial_r (\psi \partial_r w) = -p - \frac{F}{2\pi} \frac{\delta(r)}{r}, \quad (3)$$

$$\frac{1}{Y} r \partial_r \left[\frac{1}{r} \partial_r (r \psi) \right] = \frac{r}{R_0} \partial_r w - \frac{1}{2} (\partial_r w)^2 \quad (4)$$

(with $\nabla^2 \dots = (\frac{1}{r} \partial_r) + \partial_r^2 \dots = \frac{1}{r} \partial_r r \partial_r \dots$). Positive p corresponds to a *compressive* pressure, a positive F corresponds to a compressive point force, and the point force acts at $r = 0$. The first equation, (3), is the force balance in vertical direction, and the second equation, (4), is the (integrated) compatibility of strains. The in-plane stresses are obtained as $\sigma_{\phi\phi} = \psi'$ and $\sigma_{rr} = \psi/r$. We assume thin shells $h/R_0 \ll 1$ and shallow shells, i.e., small slopes $|w'| \ll 1$ [46], in the above equations.

Equations (3) and (4) have to be solved with boundary conditions $w(\infty) = w'(\infty) = 0$ and $\psi(\infty) = 0$ (or $\psi'(\infty) = 0$) for $r \rightarrow \infty$; at $r = 0$, we require a given indentation $w(0) < 0$, $w'(0) = 0$ corresponding to the

absence of kinks, and $\lim_{r \rightarrow 0} (r \psi'(r)) - \nu \psi(0) = 0$ corresponding to vanishing radial in-plane displacement to avoid tearing the shell. We prescribe the indentation $w(0) < 0$ at the origin, solve Eq. (3) in the domain $r > 0$ where $F = 0$, and calculate the necessary force F to induce this indentation only afterward from an integrated version of Eq. (3) [19, 52].

In the absence of a point force, the pressure p puts the shell into a uniformly pre-compressed state with $w(r) = w_0 < 0$ and $\psi(r) = \psi_0(r) = -pR_0 r/2$ corresponding to stresses $\sigma_{rr} = \sigma_{\phi\phi} = \sigma_0 = -pR_0/2$. We consider changes with respect to this precompressed state and substitute $w(r) \rightarrow w_0 + w(r)$ and $\psi(r) \rightarrow \psi_0(r) + \psi(r)$, such that Eq. (3) becomes

$$\begin{aligned} \kappa \nabla^4 w + \frac{1}{R_0} \frac{1}{r} \partial_r (r \psi) - \sigma_0 \nabla^2 w - \frac{1}{r} \partial_r (\psi \partial_r w) \\ = -\frac{F}{2\pi} \frac{\delta(r)}{r} \end{aligned} \quad (5)$$

while Eq. (4) remains unchanged. The boundary conditions for $w(r)$ and $\psi(r)$ are unchanged by this substitution, and we define the indentation depth z ($z > 0$) at the pole with respect to the precompressed state; i.e., we require $w(0) = -z < 0$ at $r = 0$ after substitution. The additional term $+\sigma_0 \nabla^2 w$ in Eq. (5) induces a tendency of the precompressed state for oscillating w fluctuations as it is the variation of an effective energy $-\frac{1}{2} \sigma_0 \int d^2 \mathbf{r} (\nabla w)^2$, which is lowered by oscillating w modes. This is the driving force for the classical instability with respect to oscillatory w modes at the buckling pressure p_c .

We introduce dimensionless quantities

$$\begin{aligned}\bar{w} &\equiv w/(\kappa/Y)^{1/2}, \quad \rho \equiv r/(\kappa R_0^2/Y)^{1/4}, \\ \bar{\psi} &\equiv \psi/(\kappa^2 Y/R_0^2)^{1/4}, \quad \bar{E} \equiv E/2\pi(\kappa^3/YR_0^2)^{1/2};\end{aligned}\quad (6)$$

i.e., we measure normal displacements w (and indentations z at the pole) in units of $(\kappa/Y)^{1/2} = R_0\gamma^{-1/2} = hk^{-2}$, which is, apart from factors of $k \equiv [12(1-\nu^2)]^{1/4}$, the shell thickness h (the dimensionless radius is thus $\bar{R}_0 = \gamma^{1/2}$), radial distances in units of the elastic length scale $l_{el} = (\kappa R_0^2/Y)^{1/4} = R_0\gamma^{-1/4} = (hR_0)^{1/2}k^{-1}$ (the radial scale on which bending and stretching energy are balanced), which is also the unstable wave length at the buckling transition at p_c [13], normal forces in units of $\kappa/R_0 = YR_0\gamma^{-1}$, and energies in units of $2\pi(\kappa^3/YR_0^2)^{1/2} = 2\pi YR_0^2\gamma^{-3/2}$. The dimensionless shallow shell equations (5) and (4) become

$$\nabla_\rho^4 \bar{w} + \frac{1}{\rho} \partial_\rho(\rho \bar{\psi}) + 2 \frac{p}{p_c} \nabla_\rho^2 \bar{w} - \frac{1}{\rho} \partial_\rho(\bar{\psi} \partial_\rho \bar{w}) = -\frac{\bar{F}}{2\pi} \frac{\delta(\rho)}{\rho}, \quad (7)$$

$$\rho \partial_\rho \left[\frac{1}{\rho} \partial_\rho(\rho \bar{\psi}) \right] = \rho \partial_\rho \bar{w} - \frac{1}{2} (\partial_\rho \bar{w})^2 \quad (8)$$

with $\nabla_\rho^2 \dots = \frac{1}{\rho} \partial_\rho(\rho \partial_\rho \dots)$, and $\bar{F} \equiv F\gamma/YR_0$. We compare to other non-dimensionalization schemes of the problem in Table I in Appendix C. Shallow shell theory is applicable as long as $\partial_r w \ll 1$ [46], which implies $\partial_\rho \bar{w} \ll \gamma^{1/4}$ in dimensionless quantities.

A. Exact analytical results

Because $\bar{w}(\rho)$ decays exponentially for $\rho \gg 1$, we can obtain

$$\bar{\psi} \sim -\bar{F}/2\pi\rho \quad \text{for } \rho \rightarrow \infty \quad (9)$$

from integrating (7) over a circle of radius $\rho \rightarrow \infty$ on both sides, $\int_0^\rho d\tilde{\rho} \tilde{\rho} \dots$, resulting in $\tilde{\rho} \bar{\psi}|_0^\rho \sim \rho \bar{\psi} = -\frac{\bar{F}}{2\pi}$ [52]. Equation (9) also follows from force balance in the point force direction [19].

From the shallow shell equations (7) and (8), two exact relations can be obtained. Multiplying by ρ and integrating from ρ to infinity on both sides of Eq. (7) and using (9) at infinity gives the first relation

$$-\rho \partial_\rho(\nabla_\rho^2 \bar{w}) - \rho \bar{\psi} + \bar{\psi} \partial_\rho \bar{w} - 2 \frac{p}{p_c} \rho \partial_\rho \bar{w} = \frac{\bar{F}}{2\pi}. \quad (10)$$

Dividing by ρ and integrating from ρ to infinity on both sides of Eq. (8), multiplying by ρ and integrating from 0 to infinity on both sides, and using (9) at infinity and one partial integration on the right-hand side give the second relation

$$-\frac{\bar{F}}{2\pi} = \int_0^\infty d\rho \rho \bar{w} + \int_0^\infty d\rho \rho \frac{1}{4} (\partial_\rho \bar{w})^2. \quad (11)$$

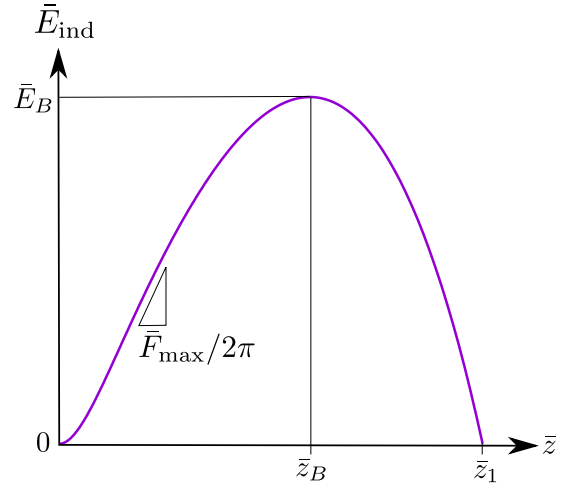


FIG. 2. Schematic energy landscape \bar{E}_{ind} as a function of indentation depth \bar{z} . The indentation at the energy barrier maximum is \bar{z}_B , the height of the energy barrier is \bar{E}_B . At depth \bar{z}_1 , unindented and indented state have equal energies.

Both of these equations can be employed to determine the point force \bar{F} for a given indentation \bar{z} and thus the force-indentation relation $\bar{F} = \bar{F}(\bar{z})$ numerically.

The force-indentation relation can be integrated to obtain the indentation energy \bar{E}_{ind} as a function of the indentation depth, $\bar{E}_{\text{ind}}(\bar{z}) = \frac{1}{2\pi} \int_0^{\bar{z}} \bar{F}(\tilde{z}) d\tilde{z}$. We note that this is the total energy difference with respect to the precompressed spherical state (at pressure p) if an additional indentation of depth \bar{z} is generated (by applying a point force \bar{F}). At the barrier state, the indentation energy has a maximum as a function of the indentation \bar{z} . If we call the indentation in the barrier state \bar{z}_B (see Fig. 1), it fulfills $\partial \bar{E}_{\text{ind}} / \partial \bar{z}(\bar{z}_B) = 0$ or $\bar{F}(\bar{z}_B) = 0$. We introduce the barrier energy as energy difference between barrier state and the precompressed spherical state, $\bar{E}_B = \bar{E}_{\text{ind}}(\bar{z}_B)$. Vice versa, the force-indentation relation $\bar{F} = \bar{F}(\bar{z})$ is obtained from the energy $\bar{E}_{\text{ind}}(\bar{z})$ by minimizing the tilted indentation energy landscape $\bar{E}_{\text{ind}}(\bar{z}) - \bar{F}\bar{z}/2\pi$. The slope of the energy landscape $\bar{E}_{\text{ind}}(\bar{z})$ at \bar{z} gives the necessary point force $\bar{F}/2\pi$ to achieve an indentation \bar{z} . A pushing compressive point force is necessary to achieve indentations where the energy landscape is increasing; at the maximum in the barrier state a force-free unstable equilibrium is achieved; at indentations where the energy landscape decreases, the shell can only be stabilized by a pulling point force. Figure 2 summarizes important features of a schematic buckling energy landscape.

The energy barrier, i.e., the difference in total energy $\Delta E_{\text{tot}} = \Delta E_s + \Delta E_b + p\Delta V$ (the sum of stretching, bending, and mechanical pressure work) between barrier state and the precompressed spherical state is given by the simple, explicit formula

$$\bar{E}_B = \Delta \bar{E}_{\text{tot}} = -\frac{1}{4} \int_0^\infty d\rho \bar{\psi} (\partial_\rho \bar{w})^2, \quad (12)$$

where $\bar{\psi}$ and \bar{w} are solutions of the shallow shell equations (7) and (8) for $\bar{F} = 0$. Equation (12) is derived in Appendix A. This result allows direct numerical access to the value of the energy barrier. Moreover, it will allow us to obtain analytical results both for the critical behavior of the energy barrier close to p_c , i.e., for shallow barriers with small indentations $\bar{z} \ll 1$ and for $p \gg p_c$, i.e., for barrier states with deep indentations $\bar{z} \gg 1$, which are mirror-inverted Pogorelov dimples. Equation (12) actually gives a positive energy because there is mainly compressive hoop stress ($\bar{\psi} < 0$) in the regions where $(\partial_\rho \bar{w})^2 > 0$ is large, i.e., at the rim of the indentation. For a Pogorelov dimple, this is exactly the inner rim of the Pogorelov ridge [44, 45] [see also Fig. 4(c)].

The terms in the second exact relation (11) are directly related to the dimensionless volume change by indentation, $\overline{\Delta V} = \Delta V / (\kappa R_0 / Y)$, and the dimensionless area change by indentation, $\overline{\Delta A} = \Delta A / (\kappa / Y)$,

$$\overline{\Delta V} \approx 2\pi \int_0^\infty d\rho \rho \bar{w} < 0 \quad (13)$$

$$\overline{\Delta A} \approx 2\pi \int_0^\infty d\rho \rho \left[2\bar{w} + \frac{1}{2}(\partial_\rho \bar{w})^2 \right], \quad (14)$$

where we work in shallow shell approximation, i.e., assuming $w/R \ll \partial_r w \ll 1$ or $\bar{w}\gamma^{-1/2} \ll \partial_\rho \bar{w}\gamma^{-1/4} \ll 1$. Therefore, relation (11) is equivalent to a relation

$$-\bar{F} = -\frac{\partial \bar{E}_{\text{ind}}}{\partial \bar{z}} = \frac{1}{2} \overline{\Delta A} \quad (15)$$

for the area change by point force indentation. This implies that the area is decreased ($\Delta A < 0$) by a compressive point force indentation or an increasing indentation energy up to the barrier, whereas it is increased ($\Delta A > 0$) for a decreasing indentation energy. It also shows that the force-indentation relation $\bar{F}(\bar{z}) = \partial \bar{E}_{\text{ind}} / \partial \bar{z}(\bar{z})$ directly gives the area change $\overline{\Delta A}(\bar{z}) = -\bar{F}(\bar{z})/2$ as a function of indentation. Right at the barrier state with $\bar{F} = 0$, the area change by indentation exactly vanishes,

$$0 = -\frac{\partial \bar{E}_{\text{ind}}}{\partial \bar{z}}(\bar{z}_B) = \frac{1}{2} \overline{\Delta A}(\bar{z}_B). \quad (16)$$

The mirror-inverted Pogorelov dimple exactly fulfills this requirement by definition but this result not only holds in the Pogorelov limit $p/p_c \ll 1$ but for all pressures p . In particular, it also holds close to p_c , where the barrier state does not resemble a Pogorelov dimple but becomes shallow and oscillatory. At the maximal point force \bar{F}_{max} , which has to be applied to overcome the energy barrier and which is the characteristic maximal point force for structural stability below p_c (see Fig. 2), the shell area is minimal, and $-\bar{F}_{\text{max}} = \frac{1}{2} \overline{\Delta A}_{\text{min}}$.

After nondimensionalization (6), the shallow shell equations (7) and (8) only depend on the parameters p/p_c and \bar{F} , which is a function of the indentation depth \bar{z} . Therefore, properties of the barrier state that can be directly obtained from solution of the dimensionless shallow shell equations, such as the dimensionless indentation

\bar{z}_B , will only depend on p/p_c . Because the dimensionless energy barrier \bar{E}_B can also be expressed directly by solutions of the shallow shell equations at $\bar{F} = 0$ via Eq. (12), also \bar{E}_B will only depend on p/p_c , see our main results (33) and (53) below. In particular, \bar{E}_B does not depend on the Poisson number ν in shallow shell theory.

B. Numerical method

We solve the nonlinear shell theory boundary problem (7) and (8) numerically on a finite domain $\rho_{\text{min}} < \rho < \rho_{\text{max}}$ ($\rho_{\text{min}} = 10^{-5}$, $\rho_{\text{max}} = 5000$) using the MATLAB routine `bvp4c` with boundary conditions $\bar{w}(\rho_{\text{max}}) = \bar{w}'(\rho_{\text{max}}) = 0$ and $\bar{\psi}'(\rho_{\text{max}}) = -\bar{\psi}(\rho_{\text{max}})/\rho_{\text{max}}$ at “infinity”; the last condition is crucial to enforce the correct asymptotics $\bar{\psi} \propto 1/\rho$ [see Eq. (9)]. At “ $\rho = 0$ ”, we use $\rho_{\text{min}}\bar{\psi}'(\rho_{\text{min}}) - \nu\bar{\psi}(\rho_{\text{min}}) = 0$ for vanishing radial in-plane displacement (with $\nu = 1/3$), $\bar{w}'(\rho_{\text{min}}) = 0$, and a prescribed indentation depth $\bar{w}(\rho_{\text{min}}) = -\bar{z} < 0$ instead of the point force, which is absent in the domain $\rho > 0$ [19, 52].

Inserting the numerical solution into Eqs. (10) (which holds pointwise for each ρ but is used after averaging over all ρ) or (11) gives the value of the force \bar{F} for the prescribed indentation depth \bar{z} , which allows us to scan the force-indentation relation $\bar{F} = \bar{F}(\bar{z})$ by gradually increasing \bar{z} . Knowledge of the entire force-indentation relation $\bar{F}(\bar{z})$ enables us to calculate the energy barrier by numerical integration $\bar{E}_B = \frac{1}{2\pi} \int_0^{\bar{z}_B} \bar{F}(\bar{z}) d\bar{z}$ up to the barrier indentation \bar{z}_B where the force vanishes, $\bar{F}(\bar{z}_B) = 0$.

While calculation of the entire force-indentation relation and numerical integration up to the barrier state where $\bar{F}(\bar{z}_B) = 0$ is an intuitive approach, there is a much more efficient way to numerically calculate the energy barrier: The exact result (12) can be employed to evaluate the energy barrier directly for a barrier state with $\bar{F} = 0$. To obtain the energy barrier as a function of p , we continue numerical solutions of the shallow shell equations (7) and (8) for the barrier states with $\bar{F} = 0$ for small changes in p and evaluate the energy barrier directly at each barrier state using (12). This supersedes calculation of the entire force-indentation relation $\bar{F}(\bar{z})$ in order to calculate a single energy barrier value by numerical integration of the force-indentation relation. We checked that we obtain numerically identical results with both methods.

III. LINEAR RESPONSE, SHELL STIFFNESS, AND SOFTENING CLOSE TO BUCKLING

Many mechanical compression tests such as plate compression [49, 50] or compression by microscopy tips [50, 51] are equivalent to point force indentation in the initial small displacement regime, which can be described by linear response. We will rederive the linear stiffness of

the shell and show that the result for a pressurized spherical shell with $p > 0$ [52] can be continued to compressive pressures $0 < p < p_c$.

Linearizing Eqs. (7) and (8) gives the Reissner equations [16, 52, 54]

$$\begin{aligned} \nabla_\rho^4 \bar{w} - \nabla_\rho^2 \bar{\Phi} + 2 \frac{p}{p_c} \nabla_\rho^2 \bar{w} &= -\frac{\bar{F}}{2\pi} \frac{\delta(\rho)}{\rho}, \\ \nabla_\rho^4 \bar{\Phi} &= -\nabla_\rho^2 \bar{w} \end{aligned} \quad (17)$$

with the dimensionless Airy stress function $\bar{\Phi}$ ($\bar{\psi} = -\partial_\rho \bar{\Phi}$). In the domain $\rho > 0$, where the δ -function on the right-hand side vanishes, these equations can be solved using the original ansatz of Reissner [54], $f_\pm \equiv \bar{w} + \lambda_\mp \bar{\Phi}$, which decouples equations to $\nabla_\rho^4 f_\pm - \lambda_\pm \nabla_\rho^2 f_\pm = 0$ if $\lambda_\pm = -p/p_c \pm i(1 - (p/p_c)^2)^{1/2}$ ($\lambda_+ \lambda_- = 1$). This finally leads to solutions

$$\bar{w}_{\text{lin}} = \frac{\bar{z}}{\ln \lambda_+} \left(K_0(\lambda_+^{1/2} \rho) - K_0(\lambda_-^{1/2} \rho) \right), \quad (18a)$$

$$\begin{aligned} \bar{\Phi}_{\text{lin}} &= \frac{\bar{z}}{\ln \lambda_+} \left(\lambda_+ K_0(\lambda_-^{1/2} \rho) - \lambda_- K_0(\lambda_+^{1/2} \rho) \right. \\ &\quad \left. + (\lambda_+ - \lambda_-) \ln \rho \right), \end{aligned} \quad (18b)$$

$$\begin{aligned} \bar{\psi}_{\text{lin}} &= -\frac{\bar{z}}{\ln \lambda_+} \left(\lambda_-^{1/2} K_1(\lambda_+^{1/2} \rho) - \lambda_+^{1/2} K_1(\lambda_-^{1/2} \rho) + \right. \\ &\quad \left. + \frac{\lambda_+ - \lambda_-}{\rho} \right) \end{aligned} \quad (18c)$$

satisfying all boundary conditions.

The force \bar{F} for given \bar{z} and thus the force-indentation relation in the linear approximation remains to be determined. It can be obtained from Eq. (11) by neglecting the last term, which is quadratic in \bar{z} ,

$$\begin{aligned} -\frac{\bar{F}(\bar{z})}{2\pi} &= \int_0^\infty d\rho \rho \bar{w}_{\text{lin}} = \bar{z} \frac{\lambda_- - \lambda_+}{\ln \lambda_+} \\ &\approx -\frac{2\sqrt{2}\bar{z}}{\pi} (1 - p/p_c)^{1/2}, \end{aligned} \quad (19)$$

where the last approximation holds for $p \approx p_c$. Alternatively, we can inspect the asymptotics of the linear solution (18c) for $\rho \rightarrow \infty$,

$$\bar{\psi}_{\text{lin}} = -\partial_\rho \bar{\Phi}_{\text{lin}} \approx \bar{z} \frac{\lambda_- - \lambda_+}{\ln \lambda_+} \frac{1}{\rho}, \quad (20)$$

which should be $\bar{\psi} \sim -\bar{F}/2\pi\rho$ according to (9) or (10). Both (19) and (20) lead to the same dimensionless linear stiffness

$$\bar{k} = \frac{d\bar{F}}{d\bar{z}} = \frac{4\pi i(1 - \tau^2)^{1/2}}{\ln(\tau + i(1 - \tau^2)^{1/2})} = \frac{4\pi(1 - (p/p_c)^2)^{1/2}}{\pi/2 + \arcsin(p/p_c)} \quad (21)$$

$$\approx 4\sqrt{2}(1 - p/p_c)^{1/2}, \quad (22)$$

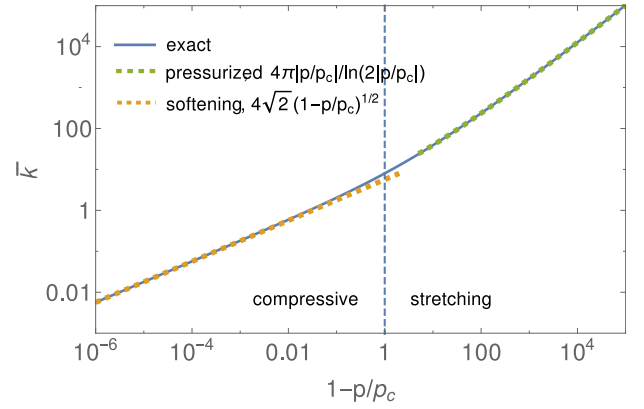


FIG. 3. Double logarithmic plot of dimensionless linear stiffness \bar{k} as a function of pressure $1 - p/p_c$ according to Eq. (21) both in the stretching ($1 - p/p_c > 1$) and compressive ($1 - p/p_c < 1$) regimes (solid blue line). For $p = 0$ (vertical dashed line), we have $\bar{k} = 8$. Dashed lines are the asymptotic results for $\bar{k} \approx 4\pi|p/p_c|/\ln(2|p/p_c|)$ in the stretching regime (right green line) and $\bar{k} \propto (1 - p/p_c)^{1/2}$ in the compressive regime (left orange line); see Eq. (22).

where $\tau \equiv -p/p_c$ and with an arcsin branch $-\pi/2 \leq \arcsin x \leq \pi/2$. Reverting the nondimensionalization we find the stiffness $k = Y\gamma^{-1/2}\bar{k}(p/p_c) = (Y^{1/2}\kappa^{1/2}/R_0)\bar{k}(p/p_c)$. In Ref. [52], the same result has been obtained for stretching pressures $p \leq 0$ ($\tau \geq 0$). We thus conclude that this result can be analytically continued also to compressive pressures $0 < p/p_c < 1$. The stiffness (22) *vanishes* as $\bar{k} \propto (1 - p/p_c)^{1/2}$ close to p_c corresponding to a softening of the capsule upon approaching the critical buckling pressure. Figure 3 clearly shows that the linear stiffness (21) is monotonously decreasing with compressive pressure p and exhibits essentially *two* scaling regimes, one for stretching pressures $-p/p_c \gg 1$, where $\bar{k} \approx 4\pi|p/p_c|/\ln(2|p/p_c|)$ [52] and the softening regime $\bar{k} \propto (1 - p/p_c)^{1/2}$ close to p_c according to (22). The crossover between both regime happens around the pressure-free case, where the Reissner results $\bar{k} = 8$ applies [54].

The linear stiffness k can be tested in various compression experiments in the initial small displacement regime. For microcapsules, most frequently used are plate compression [49, 50, 55] or compression by microscopy tips [50, 51]. In Ref. [55], the result for the stiffness (21) could also be generalized if additional surface tensions are present, which can arise, for example, from the shell-liquid interfaces or also as motor-induced active pressures if biological cells are considered [37] and which effectively act as an additional stretching pressure. Our result for the linear softening of shells could be experimentally tested in linear compression tests, where an additional compressive pressure $0 < p < p_c$ is applied.

The fact that $k > 0$ for all $p < p_c$ implies that the barrier condition $\bar{F} = 0$ can only be fulfilled for vanishing

indentations at $p = p_c$; therefore, the barrier state is *not* directly accessible in the linear response regime, and we will have to employ an additional expansion around the linearized solutions.

Close to p_c the linearized solutions (18a) and (18c) approach ($\lambda_{\pm}^{1/2} \approx \pm i$)

$$\bar{w}_{\text{lin}} \approx \frac{\bar{z}}{i\pi} (K_0(i\rho) - K_0(-i\rho)) = -\bar{z}J_0(\rho), \quad (23)$$

$$\bar{\psi}_{\text{lin}} \approx -\bar{w}'_{\text{lin}} \approx -\bar{z}J_1(\rho), \quad (24)$$

where $J_\nu(x)$ and $K_\nu(x)$ are Bessel functions. The normal displacement thus exhibits extended oscillations with a period $\Delta\rho \approx 2\pi$ corresponding to $\Delta r = 2\pi l_{\text{el}}$. This is reminiscent of the appearance of an unstable wavelength $\lambda_c = 2\pi l_{\text{el}}$ at the buckling threshold $p = p_c$ in the absence of an additional point force which localizes the dimple [13].

IV. NUMERICAL RESULTS FOR THE BARRIER STATE

Figure 1 shows numerical results for the shell configuration in the barrier state, and Fig. 4 shows the normalized displacement $\bar{w}(\rho)/\bar{z}_B$, the stress function, and stress distribution along the shell for various pressures.

In the following, we present numerical results for the energy barrier \bar{E}_B and the corresponding pole indentation \bar{z}_B at the barrier state (the indentation, where $\bar{F}(\bar{z}_B) = 0$) as a function of pressure. The scaling of these quantities with pressure starting from p close to p_c down to $p/p_c \ll 1$ always shows a clear crossover between *two* scaling regimes. One scaling regime governs the softening behavior close to p_c and characterizes the critical properties and exponents of the buckling instability; the other scaling regime for $p/p_c \ll 1$ corresponds to a barrier state, which is a well-developed mirror-inverted Pogorelov dimple. The crossover between both regimes takes place at $\bar{z}_B \sim 1$ corresponding to $z_B \sim h$ or pressures $p/p_c \sim 1/2$.

For $p \ll p_c$, we find the typical Pogorelov scaling for the energy barrier. Here, the indentation at the barrier state is deep ($\bar{z}_B \gg 1$) and typically an inverted spherical cap which is localized to $\rho < \rho_B \sim \bar{z}_B^{1/2}$; see also Fig. 4(a). For $p \ll p_c$, a deep indentation by a point force is necessary to carry the shell into the snap-through buckled state. The Pogorelov dimple consists of a mirror inverted spherical cap whose sharp edge at the rim becomes rounded to avoid infinite bending energies [18]. This rounding happens over a boundary layer of width $\xi \sim R_0\gamma^{-1/4}k = (hR_0)^{1/2} \sim l_{\text{el}}k$ [44, 45] or, in dimensionless units, $\bar{\xi} \sim k \sim O(1)$. For $\bar{z}_B < 1$ or $\rho_B < 1$ (corresponding to larger pressures $p/p_c > 1/2$), the Pogorelov dimple at the barrier state becomes too shallow to fully develop this boundary layer, and a crossover to the softening regime happens close to p_c .

Close to p_c , not only the linear stiffness k vanishes. Also the energy barrier, which protects the unbuckled

state from spontaneous buckling, and the corresponding indentation \bar{z}_B at the barrier state must vanish at p_c in order to connect smoothly to an unstable energy landscape with $\partial_z E_{\text{tot}}(z=0) < 0$ corresponding to a spontaneous buckling instability for $p > p_c$. In this regime, the indentation $\bar{w}(\rho)$ in the barrier state is very shallow [see Fig. 4(a)] and exhibits extended oscillations on the typical length scale $\Delta\rho \sim 1$ corresponding to $\Delta r \sim l_{\text{el}}$ reminiscent of the linearized theory. If p is already close to p_c , a small additional localized indentation by a point force is sufficient to carry the shell over the energy barrier into the snap-through buckled state.

After presenting the numerical results along with some scaling arguments we will derive exact analytical results for the asymptotics of the barrier energy \bar{E}_B and the barrier indentation \bar{z}_B in both limits close to p_c and for $p \ll p_c$ in the following sections.

A. Indentation in the barrier state

Close to p_c the indentation in the barrier state becomes small $\bar{z}_B \ll 1$, such that it resembles the oscillating linearized solutions (18a) and (18b). For $p \gg p_c$, on the other hand, also the barrier state is a mirror-inverted Pogorelov dimple with $\bar{z}_B \gg 1$. Many of its scaling properties can be explained based on the Pogorelov approach in this regime [9]. Figure 5 shows numerical shallow shell results for the relation between \bar{z}_B and pressure p/p_c .

Close to p_c , the indentation \bar{z}_B at the barrier [$\bar{F}(\bar{z}_B) = 0$] becomes small, $\bar{z}_B \ll 1$. Numerically, we find for \bar{z}_B as a function of pressure a crossover between just two scaling regimes,

$$\bar{z}_B \propto \begin{cases} (1 - p/p_c)^{1/2} & \text{for } p \approx p_c \\ (p/p_c)^{-2} & \text{for } p \ll p_c \end{cases}, \quad (25)$$

with a clear crossover at $\bar{z}_B \sim 1$; see Fig. 5(b). The indentation \bar{z}_B at the barrier is monotonously decreasing as a function of p , which shows that increasingly deep indentations are necessary to reach the metastable barrier beyond which the shell will spontaneously fall into the snap-through buckled state.

Both scaling results in the limits p close to p_c and $p \ll p_c$ are non-trivial results, which we will rationalize in the course of this paper. In Fig. 5, we compare with the exact asymptotics including numerical prefactors that will be calculated in the following sections and find excellent agreement. We also see that the numerical data given in Refs. [7, 10] is in excellent agreement but does not cover the asymptotics for p close to p_c . The scaling of the depth of the barrier state for $p \ll p_c$ has been obtained previously in Ref. [16] based on the Pogorelov energy estimate and in Refs. [20, 21] using a boundary layer approach with variational energy minimization that turns out to be equivalent to the systematic expansion that we will employ below.

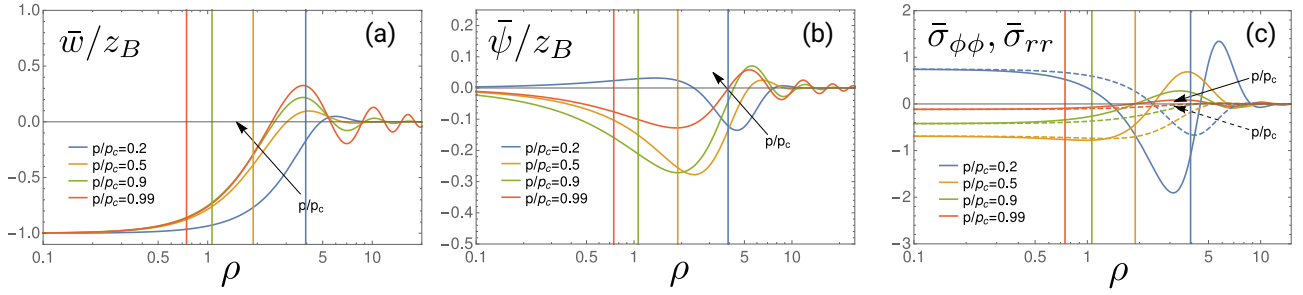


FIG. 4. Numerical results for the barrier state of a buckled spherical shell (see also shapes in Fig. 1). Arrows indicate increasing pressure. (a) Normalized dimensionless normal displacement $\bar{w}(\rho)/\bar{z}_B$, (b) normalized dimensionless stress function $\bar{\psi}(\rho)/\bar{z}_B$, and (c) dimensionless hoop stress $\bar{\sigma}_{\phi\phi} = \partial_\rho \bar{\psi}$ (solid lines) and radial stress $\bar{\sigma}_{rr} = \bar{\psi}/\rho$ (dashed lines); vertical lines indicate the indentation width $\rho_B = (2\bar{\Delta V}_B/\pi\bar{z}_B)^{1/2}$.

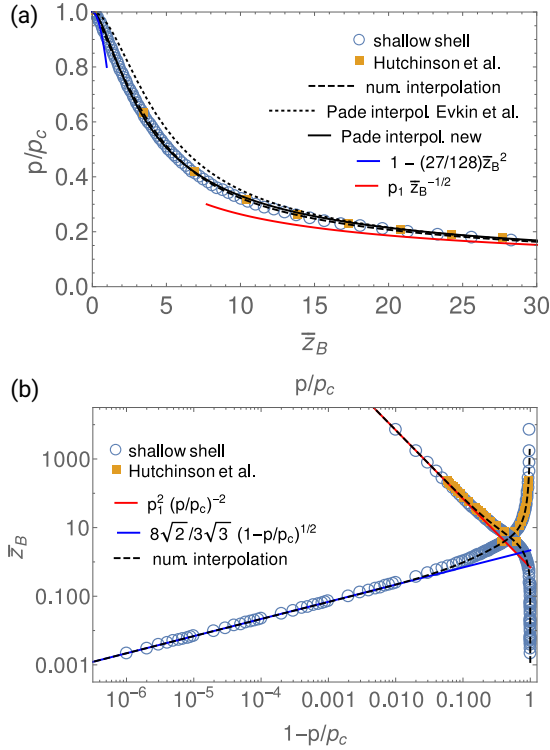


FIG. 5. Numerical shallow shell results for relation between indentation \bar{z}_B at the barrier state and pressure p/p_c . (a) Pressure p/p_c as a function of \bar{z}_B together with the asymptotic analytical results (46) (lower solid red line, $p_1 \simeq 0.8337$) and (64) (upper solid blue line). (b) Double logarithmic plot of \bar{z}_B as a function of p/p_c (upper curve and upper horizontal scale) together with the analytical result (33a) (upper solid red line) and as a function of $1 - p/p_c$ (lower curve and lower horizontal scale) together with the analytical result (53a) (lower solid blue line). In both panels (a) and (b), we also show the interpolation formula (74) (black dashed line) and the data for the function $p/p_c = f(\xi)$ versus $\bar{z}_B = \sqrt{12}\xi$ from Hutchinson *et al.* [7, 10]; see Table I in Appendix C. In panel (a), we also show Padé interpolations from Evkin *et al.* [21] (black dotted line) and as derived below [see Eq. (75), black solid line].

The dimensionless indentation volume $\bar{\Delta V}_B = -\bar{\Delta V}(\bar{z}_B) > 0$ [see Eq. (13)] at the barrier state shows a characteristic dependence on the indentation \bar{z}_B at the barrier:

$$\bar{\Delta V}_B \propto \begin{cases} \bar{z}_B & \text{for } \bar{z}_B \ll 1 \\ \bar{z}_B^2 & \text{for } \bar{z}_B \gg 1 \end{cases}, \quad (26)$$

see Fig. 6(a), with a clear crossover at $\bar{z}_B \sim 1$ ($z \sim h$) between shallow and deep indentations. Figures 6(a) and (b) also show that the numerical data from Refs. [7, 10] are in excellent agreement. When we combine (25) and (26), the pressure dependence of the indentation volume follows as

$$\bar{\Delta V}_B \propto \begin{cases} (1 - p/p_c)^{1/2} & \text{for } p \approx p_c \\ (p/p_c)^{-4} & \text{for } p \ll p_c \end{cases}, \quad (27)$$

in agreement with the numerical results in Fig. 6(b).

From the indentation volume $\bar{\Delta V}_B$ and the indentation depth \bar{z}_B at the barrier state, we can define an effective width ρ_B of the indentation as

$$\rho_B \equiv (2\bar{\Delta V}_B/\pi\bar{z}_B)^{1/2} \propto \begin{cases} \text{const} & \text{for } p \approx p_c \\ \bar{z}_B^{1/2} \propto (p/p_c)^{-1} & \text{for } p \ll p_c \end{cases}; \quad (28)$$

see Fig. 6(c). We choose the numerical prefactor in the definition of ρ_B such that a mirror-inverted Pogorelov dimple with $\bar{w}(\rho) = -\bar{z}_B + \rho^2$ and $\bar{\Delta V}_B = \pi\bar{z}_B^2/2$ has $\rho_B = \bar{z}_B^{1/2}$ in accordance with $\bar{w}(\rho_B) = 0$. This is exactly the behavior of $\bar{\Delta V}_B$ and ρ_B for $\bar{z}_B \gg 1$ or $p \ll p_c$. The effective indentation width ρ_B remains remarkably constant $\simeq 0.70$ for pressures p close to p_c corresponding to an indentation width $r_B \sim l_{el}$. This behavior will have interesting consequences for the buckling behavior of small soft spots. The depth \bar{z}_B is vanishing for p close to p_c such that the indentation at the barrier becomes not only increasingly shallow but also increasingly broad with a width-to-depth ratio $r_B/\bar{z}_B \propto \gamma^{1/4}(1 - p/p_c)^{-1/2}$ [note the different dimensionless units for r_B and z_B in Eq. (6)].

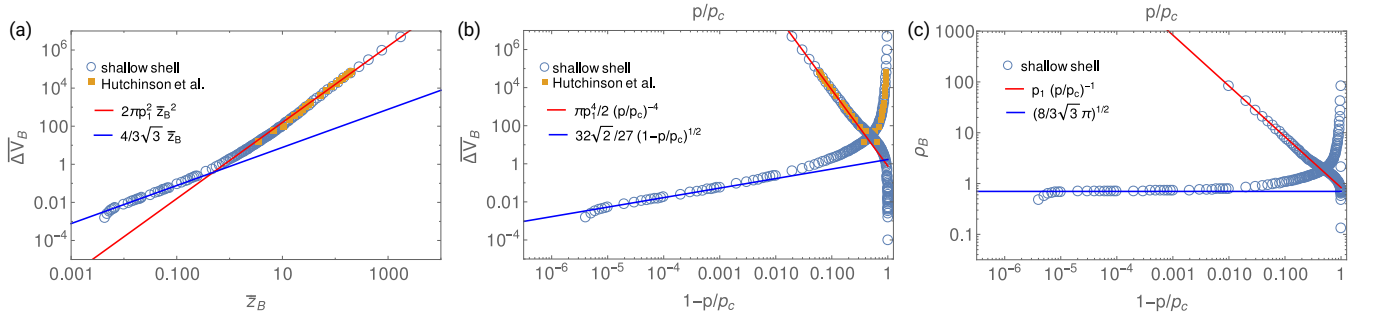


FIG. 6. Numerical shallow shell results for the indentation volume $\overline{\Delta V}_B$ and the effective indentation width $\rho_B \equiv (2\overline{\Delta V}_B/\pi\bar{z}_B)^{1/2}$ at the barrier state. (a) Dimensionless indentation volume $\overline{\Delta V}_B$ as a function of indentation depth \bar{z}_B as compared to analytical results (33b) (blue line fitting shallow indentations $\bar{z}_B \ll 1$) and (53b) (red line, $p_1 \simeq 0.8337$, fitting deep indentations $\bar{z}_B \gg 1$). (b) $\overline{\Delta V}_B/2\pi$ as a function of pressure p/p_c (upper curves and upper horizontal scale) together with analytical result (33b) (upper red line) and as a function of $1 - p/p_c$ (lower curves and lower horizontal scale) together with analytical result (53b) (lower blue line). We also show the data from Hutchinson *et al.* [7, 10] for the function $\overline{\Delta V}_B = 24\pi h(\xi)$ plotted as a function of $\bar{z}_B = \sqrt{12}\xi$ (a) or as a function of $p/p_c = f(\xi)$ and $1 - p/p_c$ (b); see Table I. (c) Effective indentation width ρ_B at the barrier state as a function of pressure p/p_c and $1 - p/p_c$ together with the analytical results (33c) (upper red line) and (53c) (lower blue line), respectively.

For $p \ll p_c$, the width of the barrier state increases with decreasing pressure such that the indentation becomes not only increasingly deep but also increasingly narrow with a depth-to-width ratio $\propto \gamma^{1/4}(p/p_c)^{-1}$.

For a Pogorelov dimple, the scaling $\overline{\Delta V}_B \sim (p/p_c)^{-4}$ has been shown in Ref. [9] based on the Pogorelov energy estimate for the elastic energy of a mirror-inverted dimple. Together with the geometric result $\overline{\Delta V}_B = \pi\bar{z}_B^2/2$ for mirror-inverted dimples, this rationalizes the numerically observed scaling (25) of the indentation for $p \ll p_c$. We will present a strict derivation in the framework of nonlinear shallow shell theory below.

Because the indentation \bar{z}_B at the barrier remains small close to p_c , the solution $\bar{w}(\rho)$ resembles the linear approximation (18a) in this regime. We can use the exact relation (11) at $\bar{F} = 0$ and see that the indentation volume [the first term on the right-hand side of relation (11)] must be given by the second term on the right-hand side which is of second order in \bar{z} . Our numerics confirm that this term can still be obtained using the linearized solution (18a) to a good approximation,

$$\begin{aligned} -\frac{\overline{\Delta V}}{2\pi} &= \frac{1}{4} \int_0^\infty d\rho \rho (\partial_\rho \bar{w})^2 \approx \frac{1}{4} \int_0^\infty d\rho \rho (\partial_\rho \bar{w}_{\text{lin}})^2 \\ &\approx -\frac{\bar{z}^2}{4\ln^2 \lambda_+} \left(1 - \ln \lambda_+ \frac{\lambda_+ + \lambda_-}{\lambda_+ - \lambda_-} \right) \\ &\approx \frac{\bar{z}^2}{4\sqrt{2}\pi} (1 - p/p_c)^{-1/2} \end{aligned} \quad (29)$$

for $\bar{z} \ll 1$. The numerical results (26), (27), and (25) suggest, on the other hand, that

$$-\frac{\overline{\Delta V}}{2\pi} = - \int_0^\infty d\rho \rho \bar{w} = \text{const } \bar{z} \quad (30)$$

still holds at the barrier, i.e., that the term is still linear in \bar{z} to a good approximation and the indentation extends

over $\rho = O(1)$. The indentation volume does, however, not contain a factor $(1 - p/p_c)^{1/2}$ as in the linearized solution [see Eq. (19)]. Nonlinear corrections are affecting the shape of the indentation at the barrier such that the cancellation of oscillating contributions that governs the linearized result (19) no longer happens but the indentation still extends over $\rho = O(1)$ as in the linearized solution. Equating with Eq. (29) at the barrier gives

$$\bar{z}_B \propto (1 - p/p_c)^{1/2},$$

which explains the numerically observed scaling (25) of the indentation close to p_c . We will present a strict derivation in the framework of nonlinear shallow shell theory below.

B. Energy barrier

Now we address the energy barrier itself. Numerically, we find for the energy barrier height

$$\bar{E}_B \propto \begin{cases} \bar{z}_B^3 & \text{for } \bar{z}_B \ll 1 \\ \bar{z}_B^{3/2} & \text{for } \bar{z}_B \gg 1 \end{cases}, \quad (31)$$

again with clearly two regimes and a crossover at $\bar{z}_B \sim 1$, see Fig. 7(a). For small indentations $\bar{z} \ll 1$, the linear regime with $\bar{\psi}, \bar{w} \propto \bar{z}$ is a good approximation up to the barrier, and the typical radial extent of the indentation is $\rho = O(1)$, resulting in $\bar{E}_B \propto \bar{z}_B^3$ according to (12). For deep indentations $\bar{z} \gg 1$, the characteristic behavior of a mirror-inverted Pogorelov dimple is $\partial_\rho \bar{w} \sim \bar{z}^{1/2}$ and $\bar{\psi} \sim \bar{z}^{1/2}$ over a width $\Delta\rho = O(1)$ at $\rho \sim \bar{z}^{1/2}$ (in the absence of pressure) [19], which results in $\bar{E}_B \propto \bar{z}_B^{3/2}$ according to (12). This means both scaling limits in (31) can be rationalized by nonlinear shallow shell theory. In Fig.

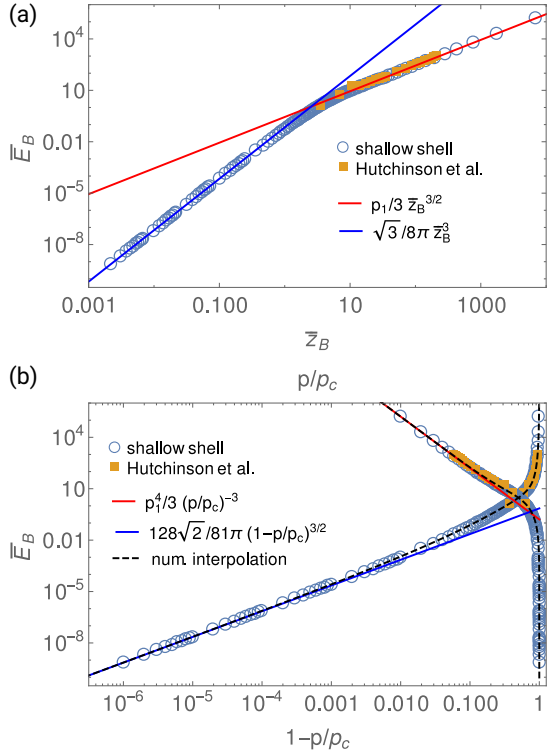


FIG. 7. Numerical shallow shell results for the energy barrier \bar{E}_B . (a) Double logarithmic plot of \bar{E}_B as a function of barrier indentation \bar{z}_B with the analytical results (33d) (red line, $p_1 \simeq 0.8337$, fitting deep indentations $\bar{z}_B \gg 1$) and (53d) (blue line fitting shallow indentations $\bar{z}_B \ll 1$). (b) Double logarithmic plot of \bar{E}_B as a function of pressure p/p_c (upper curves and upper horizontal scale) together with the analytical result (33e) (upper red line) and as a function of $1 - p/p_c$ (lower curves and lower horizontal scale) together with the analytical result (53e) (lower blue line). Also shown are the data from Hutchinson *et al.* [7, 10] and the interpolation formula (73) (black dashed line in panel (b)).

7(a), we compare with the exact asymptotics including numerical prefactors that will be calculated rigorously in the following sections.

Together with (25), this results in a pressure dependence

$$\bar{E}_B \propto \begin{cases} (1 - p/p_c)^{3/2} & \text{for } p \approx p_c \\ (p/p_c)^{-3} & \text{for } p \ll p_c \end{cases}, \quad (32)$$

in agreement with the numerical results in Fig. 7(b). The scaling $\bar{E}_B \propto (p/p_c)^{-3}$ for deep indentations has been obtained before in Refs. [9, 17, 21] (and implicitly also in Ref. [16]) based on the arguments of Pogorelov for the energy cost of a buckling indentation. The scaling $\bar{E}_B \propto (1 - p/p_c)^{3/2}$ governs the softening of the shell close to the buckling pressure and is a new result that corrects the conjecture $\bar{E}_B \propto (1 - p/p_c)^2$ that has been obtained based on numerical data from SURFACE EVOLVER simulations in Ref. [9]. The SUR-

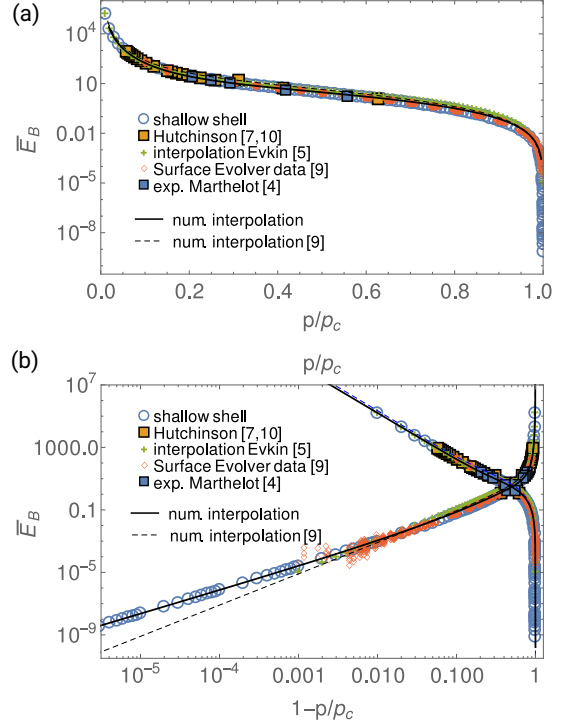


FIG. 8. Comparison of our numerical shallow shell results for the energy barrier \bar{E}_B as a function of p/p_c or $1-p/p_c$ [(a) logarithmic, (b) double-logarithmic] to different analytical, numerical, and experimental energy barrier results from the literature: numerical data from Hutchinson *et al.* [7, 10] (orange big squares), energy barrier from integrating an analytical interpolation of the force-indentation relation from Evkin *et al.* [5] (green crosses), experimental data from Marthelot *et al.* [4] (blue small squares), and SURFACE EVOLVER data (red diamonds) and an approximative numerical interpolation formula from Ref. [9] (dashed line). We also compare to the new interpolation formula (73) (solid line). Clearly, shallow shell theory is correct through the whole range of pressures.

FACE EVOLVER is, however, not well suited to investigate very shallow dimples as they occur close to p_c . Shallow shell theory and the numerical continuation approach give much better results in this regime, which extend over several decades of the small parameter $1 - p/p_c$ and reveal the actual exponent 3/2. In Fig. 8, we compare our numerical results from shallow shell theory to the SURFACE EVOLVER simulation, to numerical data from Hutchinson and coworkers from Refs. [7, 10] from moderate rotation theory, to an analytical interpolation formula from Evkin *et al.* [5], and to experimental data from Marthelot *et al.* [4]. We find excellent agreement and see that only the present numerical approach accesses the asymptotics for p close to p_c .

V. SHALLOW SHELL THEORY FOR THE POGORELOV BARRIER STATE

In this section, we derive several analytical results for the energy barrier state from nonlinear shallow shell theory in the Pogorelov limit $p \ll p_c$ corresponding to a deep indentation $\bar{z}_B \gg 1$ in the barrier state:

$$\bar{z}_B = p_1^2 (p/p_c)^{-2} + O[(p/p_c)^0], \quad (33a)$$

$$\overline{\Delta V}_B \approx \frac{\pi}{2} \bar{z}_B^2 \approx \frac{\pi p_1^4}{2} (p/p_c)^{-4}, \quad (33b)$$

$$\rho_B \approx p_1 (p/p_c)^{-1}, \quad (33c)$$

$$\bar{E}_B = \frac{p_1}{3} \bar{z}_B^{3/2} + O(\bar{z}_B), \quad (33d)$$

$$\bar{E}_B = \frac{p_1^4}{3} (p/p_c)^{-3} + O[(p/p_c)^{-2}] \quad \text{with} \quad (33e)$$

$$p_1 \simeq 0.83370854. \quad (33f)$$

Thus we derive all Pogorelov scaling exponents [see Refs. [5, 9, 17] and Eqs. (25), (26), (27), (28), (31), and (32)] from nonlinear shallow shell theory and also obtain exact numerical prefactors. The number p_1 can be written as analytic expression in terms of an integral over a solution of simple differential equations and is numerically easily accessible [see Eq. (45) below]. The prefactors accurately agree with the asymptotic numerical results; see Figs. 5, 6, and 7. We will further show that the total indentation energy landscape in the presence of pressure is given by

$$\begin{aligned} \bar{E}_{\text{ind}}(\bar{z}) &= \bar{E}_{\text{ind}, p=0}(\bar{z}) + \overline{p\Delta V}(\bar{z}) \\ &= \frac{4p_1}{3} \bar{z}^{3/2} - \frac{p}{p_c} \bar{z}^2; \end{aligned} \quad (34)$$

i.e., the pressure dependence is only via the mechanical work and the elastic part of the indentation energy $\bar{E}_{\text{ind}}(\bar{z})$ is independent of pressure. For deep dimples with $\bar{z} \gg 1$ and $p \ll p_c$, where Eq. (34) is valid, an additional pressure represents only a small perturbation which is apparently not modifying the elastic energy in leading order.

In the regime $p \ll p_c$, where the barrier state is a deep mirror-inverted dimple with $\bar{z}_B \gg 1$, we can start from the following mirror-inverted solution of shallow shell equations at the barrier $\bar{F} = 0$:

$$\begin{aligned} \bar{w}(\rho) &= \begin{cases} -\bar{z}_B + \rho^2 & \text{for } \rho < \bar{z}_B^{1/2} \\ 0 & \text{for } \rho > \bar{z}_B^{1/2}, \end{cases} \\ \bar{\psi}(\rho) &= \begin{cases} 4(p/p_c)\rho & \text{for } \rho < \bar{z}_B^{1/2} \\ 0 & \text{for } \rho > \bar{z}_B^{1/2}, \end{cases} \end{aligned} \quad (35)$$

which is an exact solution everywhere except right at the rim of the dimple at $\rho = \bar{z}_B^{1/2}$, where it exhibits discontinuities. Following Ref. [19] (where the case $p = 0$ and $\bar{F} > 0$ was considered), we smooth these discontinuities

by an ansatz ($x \equiv \rho - \bar{z}_B^{1/2}$)

$$\partial_\rho \bar{w}(\rho) = f(x) + \begin{cases} 2(\bar{z}_B^{1/2} + x) & \text{for } x < 0 \\ 0 & \text{for } x > 0, \end{cases} \quad (36a)$$

$$\bar{\psi}(\rho) = \chi(x) + \begin{cases} 4(p/p_c)(\bar{z}_B^{1/2} + x) & \text{for } x < 0 \\ 0 & \text{for } x > 0, \end{cases} \quad (36b)$$

where the functions $f(x)$ and $\chi(x)$ have discontinuities at $x = 0$ in order to lead to smooth functions \bar{w} and $\bar{\psi}$. This ansatz is conceptually similar to the boundary layer approach of Evkin *et al.* [20, 21].

As in Ref. [19], we determine f , χ , and p in an expansion in inverse powers of \bar{z}_B . Gomez *et al.* considered the Pogorelov dimple created by a point force $\bar{F} > 0$ in the absence of pressure and calculated the force-indentation curve, i.e., the point force necessary to maintain a given indentation \bar{z} . Here, we consider a metastable Pogorelov barrier state with $\bar{F} = 0$ with a given indentation \bar{z}_B and calculate the pressure p necessary to maintain such a state. A major difference between both cases is the behavior of ψ in the inner region of the dimple. Because $\bar{\psi} \sim -\bar{F}/2\pi\rho$ for a mirror-inverted Pogorelov state close to the ridge (the inner side of the ridge is compressed), this divergence of $\bar{\psi}$ for small ρ demands for the existence of four additional scaling regions in the interior of the dimple ($\rho < \sqrt{\bar{z}}$) [19], resulting in the existence of a total of seven scaling regions. For the barrier state, on the other hand, we have $\bar{F} = 0$ and this divergence of $\bar{\psi}$ is absent. Therefore, the solution (35) is valid in the entire region $\rho < \sqrt{\bar{z}_B}$ apart from the immediate ridge region and no additional regimes are present. In a sense, the original Pogorelov picture with three regions – mirror-buckled inside, Pogorelov ridge and undeformed outside – is recovered for the barrier state. Moreover, it is the existence of the additional inner regions that calls for an expansion of f , χ , and p in powers of $\bar{z}^{-1/4}$. If these regions are absent, the scaling in (36) actually suggests that an expansion in powers of $\bar{z}_B^{-1/2}$ is sufficient:

$$\begin{aligned} f(x) &= \bar{z}_B^{1/2} f_0 + f_1 + \bar{z}_B^{-1/2} f_2 + \dots, \\ \chi(x) &= \bar{z}_B^{1/2} \chi_0 + \chi_1 + \bar{z}_B^{-1/2} \chi_2 + \dots, \\ p/p_c &= p_0 + \bar{z}_B^{-1/2} p_1 + \dots \end{aligned} \quad (37)$$

In order to assure a continuous solution, $f(x)$ and $\chi(x)$ have to fulfill the following jump conditions at $x = 0$:

$$\begin{aligned} f|_{0-}^{0+} &= 2\bar{z}_B^{1/2}, \quad f'|_{0-}^{0+} = 2, \\ \chi|_{0-}^{0+} &= 4\frac{p}{p_c}\bar{z}_B^{1/2}, \quad \chi'|_{0-}^{0+} = 4\frac{p}{p_c}. \end{aligned} \quad (38)$$

Moreover, $f(x)$ and $\chi(x)$ vanish exponentially for $x \rightarrow \pm\infty$. We expect $f(x)$ and $\chi(x)$ to decay exponentially on the dimensionless length set by the width of the Pogorelov rim $\xi \sim O(1)$. We note that Evkin *et al.* [20, 21] use a conceptually similar boundary layer approach which is based on essentially the same expansion parameter $\varepsilon \sim \bar{z}_B^{-1/2}$.

A. Leading order

Inserting the expansion (37) and the ansatz (36) into the integrated force balance (10) for \bar{w} and the compatibility condition (8) for $\bar{\psi}$, we obtain in order \bar{z}_B the following differential equations for $f_0(x)$ and $\chi_0(x)$ [56]:

$$\begin{aligned} f_0'' + \operatorname{sgn}x(\chi_0 + 2p_0f_0) &= f_0\chi_0, \\ \chi_0'' - \operatorname{sgn}x f_0 &= -\frac{1}{2}f_0^2. \end{aligned} \quad (39)$$

The first equation is multiplied by f_0' , the second by χ_0' , and then both equations are subtracted and integrated once (with a vanishing integration constant because of boundary conditions at infinity) to give a first integral,

$$\frac{1}{2}(f_0'^2 - \chi_0'^2 - f_0^2\chi_0) + \operatorname{sgn}x f_0\chi_0 = -\operatorname{sgn}x p_0 f_0^2, \quad (40)$$

which holds both in $x > 0$ and $x < 0$ (but not right at $x = 0$). Subtracting this relation for $x = 0-$ from the relation at $x = 0+$ and employing the jump conditions at order $\bar{z}_B^{1/2}$,

$$\begin{aligned} f_0|_{0-}^{0+} &= 2, & f_0'|_{0-}^{0+} &= 0, \\ \chi_0|_{0-}^{0+} &= 4p_0, & \chi_0'|_{0-}^{0+} &= 0, \end{aligned} \quad (41)$$

we finally obtain the relation $2p_0[f_0(0-) + 2]^2 = 0$, from which we conclude

$$p_0 = 0.$$

For $p_0 = 0$, Eqs. (39) are symmetric such that

$$f_0(x) \text{ odd}, \quad \chi_0(x) \text{ even}.$$

This symmetry together with the discontinuities (41) also requires $f_0(0+) = 1$. A numerical solution of Eqs. (39) for $x > 0$ using the MATLAB routine `bvp4c` is shown in Fig. 9. The boundary conditions are $f_0(x_{\min}) = 1$, $\chi_0'(x_{\min}) = 0$, and $f_0(x_{\max}) = 0$, $\chi_0(x_{\max}) = 0$ (using $x_{\min} = 10^{-7}$ and $x_{\max} = 1000$). For $p_0 = 0$, the above Eqs. (39) and boundary conditions (41) become parameter free. Therefore, solutions fall off exponentially on a parameter-independent length scale $O(1)$ (see Fig. 9), which corresponds to the width of the Pogorelov rim $\xi \sim O(1)$ as argued above.

B. First order

In order $\bar{z}_B^{1/2}$, we obtain for $f_1(x)$ and $\chi_1(x)$

$$\begin{aligned} f_1'' + (\operatorname{sgn}x - f_0)\chi_1 - \chi_0 f_1 &= -f_0' - x f_0'' + \operatorname{sgn}x x \chi_0 - 2p_1 f_0 \operatorname{sgn}x, \\ \chi_1'' + (f_0 - \operatorname{sgn}x)f_1 &= -\chi_0' - x \chi_0'' + \operatorname{sgn}x x f_0, \end{aligned} \quad (42)$$

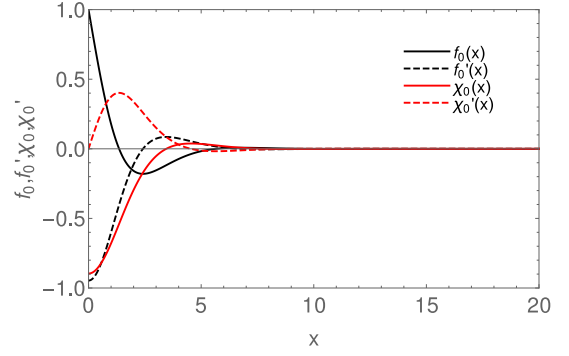


FIG. 9. Leading-order functions $f_0(x)$ and $\chi_0(x)$ (solid black and red lines) and their derivatives (dashed black and red lines) for $x > 0$ and $p_0 = 0$; on the domain $x < 0$ functions are obtained by symmetry, $f_0(x)$ and $\chi_0'(x)$ are odd, and $\chi_0(x)$ and $f_0'(x)$ are even. All functions decay exponentially on a length scale of order unity.

where we used already $p_0 = 0$. This inhomogeneous differential equation has to be solved with the jump conditions

$$\begin{aligned} f_1|_{0-}^{0+} &= 0, & f_1'|_{0-}^{0+} &= 2, \\ \chi_1|_{0-}^{0+} &= 4p_1, & \chi_1'|_{0-}^{0+} &= 4p_0 \end{aligned} \quad (43)$$

at order \bar{z}_B^0 .

Using Eq. (39), the inhomogeneous equation (42) can be written as [57]

$$\hat{L} \begin{pmatrix} f_1 \\ \chi_1 \end{pmatrix} = \begin{pmatrix} -f_0' - x f_0 \chi_0 - 2p_1 f_0 \operatorname{sgn}x \\ -\chi_0' + \frac{1}{2} x f_0^2 \end{pmatrix} \quad (44)$$

with a linear differential operator

$$\hat{L} \begin{pmatrix} f_1 \\ \chi_1 \end{pmatrix} \equiv \begin{pmatrix} f_1'' + (\operatorname{sgn}x - f_0)\chi_1 - \chi_0 f_1 \\ \chi_1'' - (\operatorname{sgn}x - f_0)f_1 \end{pmatrix}.$$

For the adjoint operator \hat{L}^+ [with respect to the scalar product $\langle (a, b), (c, d) \rangle \equiv \int_{-\infty}^{\infty} dx (a(x)c(x) + b(x)d(x))$], we can show that $\hat{L}(a, b) = 0$ is equivalent to $\hat{L}^+(a, -b) = 0$; i.e., homogeneous solutions of the problem (42) are, apart from a minus sign, also homogeneous solutions of the adjoint problem. This holds, however, only for continuous functions $a(x)$ and $b(x)$. The functions f_i and χ_i are discontinuous at $x = 0$ [see Eqs. (41) and (43)], and we have to carefully check boundary contributions.

Nevertheless, we will make use of the fact that one solution of the homogeneous problem can be explicitly constructed,

$$\hat{L} \begin{pmatrix} f_0' \\ \chi_0' \end{pmatrix} = 0 \quad \text{for } x \neq 0,$$

as can be checked by taking one derivative in the first-order equation (39). This suggests that a Fredholm solvability condition for the inhomogeneous problem (44) can be derived by forming the scalar product

$\langle (f'_0, -\chi'_0), \hat{L}(f_1, \chi_1) \rangle$ on both sides. On the left-hand side, this should give zero apart from boundary terms from $x = 0$. We find

$$\begin{aligned} \left\langle \begin{pmatrix} f'_0 \\ -\chi'_0 \end{pmatrix}, \hat{L} \begin{pmatrix} f_1 \\ \chi_1 \end{pmatrix} \right\rangle &= -f'_0 f'_{1|0-}{}^{0+} - \chi''_0 \chi'_{1|0-}{}^{0+} \\ &= -2f'_0(0) - 2p_1. \end{aligned}$$

Forming the scalar product also with the right-hand side (the inhomogeneity) of (44), using the symmetry of f_0 and χ_0 and the first integral (40) for $p_0 = 0$, integrating by parts, and using Eq. (39) for $p_0 = 0$ finally gives the following solvability condition for p_1 :

$$\begin{aligned} p_1 &= \frac{1}{4} \int_0^\infty dx (\chi_0'^2 - f_0'^2 + 2\chi_0) = -\frac{3}{5} \int_0^\infty dx \chi_0 \\ &\simeq 0.83370854, \end{aligned} \quad (45)$$

where the right-hand side has been evaluated numerically using the solutions shown in Fig. 9. The last equality of integrals is obtained by using Eq. (39) for $p_0 = 0$ after partial integration and the first integral (40) for $p_0 = 0$. Together with $p_0 = 0$, we have

$$\begin{aligned} p/p_c &= p_1 \bar{z}_B^{-1/2} + O(\bar{z}_B^{-1}), \\ \bar{z}_B &= p_1^2 (p/p_c)^{-2} + O((p/p_c)^{-1}) \end{aligned} \quad (46)$$

with $p_1^2 \simeq 0.69506993$, which is Eq. (33a). Further corrections p_2, p_3 , etc., can be calculated by extending this scheme to higher orders. Based on the symmetry properties that $f_0(x)$ and $\chi_1(x)$ are odd and $\chi_0(x)$ and $f_1(x)$ are even, we can show in the next order that

$$p_2 = 0. \quad (47)$$

This means that the leading non-vanishing corrections in Eq. (46) are actually of higher order: the leading correction to p/p_c is $O(\bar{z}_B^{-3/2})$ and the leading correction to \bar{z}_B in eq. (33a) is $O((p/p_c)^0)$. This is supported by our numerics.

The result (46) is also in agreement with the work of Evkin *et al.* [20, 21]. It can be shown that the boundary layer approach of Ref. [21] is equivalent to our expansion (37) in powers of $\bar{z}_B^{-1/2}$ (with the identification $f_0 = 2w'_1$ and $\chi_0 = -2\phi'_1$ in the notation of Ref. [21]). Evkin *et al.* use a variational approach rather than Fredholm integrability conditions to obtain the expansion coefficients p_1 and p_2 . Using the variational approach they obtain $p/p_c = (3J_0/8)\bar{z}_B^{-1/2} + O(\bar{z}_B^{-3/2})$ (see also Table I) with a numerical constant J_0 for which we can show the exact equality

$$J_0 = 2 \int_0^\infty (\chi_0'^2 + f_0'^2) = 8p_1/3, \quad (48)$$

establishing the equivalence with Eq. (46); the missing correction in order $O(\bar{z}_B^{-1})$ corresponds to $p_2 = 0$. Our numerical evaluation of p_1 gives a slightly different $J_0 \simeq$

2.22322 as compared to $J_0 \simeq 2.23$ given in Ref. [21]. We also note that the existence of only three spatial scaling regions for $\bar{\psi}$ and \bar{w} as a function of ρ in the barrier state cannot be justified systematically in the approach of Evkin *et al.*

We now return to the remarkable coincidence between our calculation for the barrier state ($\bar{F} = 0, p > 0$) and the complementary calculation by Gomez *et al.* [19] for the force-indentation curve in the absence of pressure ($p = 0, \bar{F} > 0$). Both governing differential equations (39) for the leading-order corrections f_0, χ_0 and (44) for the first-order corrections f_1, χ_1 for the Pogorelov barrier state are *identical* to the corresponding equations of Gomez *et al.* for the Pogorelov dimple with a point force in the absence of pressure. We can show that both results are exactly consistent if the elastic part of the indentation energy $\bar{E}_{\text{ind}}(\bar{z})$ is *independent of the pressure* [apart from terms of order $(p/p_c)^2$] in the Pogorelov regime $\bar{z} \gg 1$. This means that the Pogorelov dimple energy is actually independent of a precompression of the spherical shape by a pressure p , which is often tacitly assumed (for example in Refs. [9, 21]). To show this consistency, we integrate the result from Ref. [19] for the force-indentation relation in the Pogorelov limit for $p = 0, \bar{F} = F_2 \bar{z}^{1/2} + O(1)$ with $F_2/2\pi \simeq 1.6674$, to obtain the $p = 0$ indentation energy,

$$\bar{E}_{\text{ind}, p=0}(\bar{z}) = \frac{F_2}{3\pi} \bar{z}^{3/2} + O(\bar{z}^1). \quad (49)$$

If this is the elastic part of the indentation energy independent of pressure p (apart from pressure dependence in higher order terms), the only effect of an applied pressure is to add the mechanical pressure work to the total indentation energy,

$$\overline{p\Delta V} = 4 \frac{p}{p_c} \int d\rho \rho \bar{w} = \frac{2}{\pi} \frac{p}{p_c} \overline{\Delta V} \approx -\frac{p}{p_c} \bar{z}^2,$$

which is the leading-order result for a mirror-inverted dimple $\bar{w}(\rho) = -\bar{z} + \rho^2$ with $\overline{\Delta V} = -\pi \bar{z}^2/2$ [corrections should be $O(\bar{z}^1)$ if an expansion analogous to (36a) applies with an odd function $f(x)$]. The barrier state with $\bar{F} = 0$ then corresponds to an energy extremum of $\bar{E}_{\text{ind}}(\bar{z}) = \bar{E}_{\text{ind}, p=0}(\bar{z}) + p\overline{\Delta V}(\bar{z})$ with respect to variation of the indentation \bar{z} . This leads to our above result (46),

$$p/p_c = \frac{F_2}{4\pi} \bar{z}_B^{-1/2} + O(\bar{z}_B^{-1}),$$

if $p_1 = F_2/4\pi$. This is indeed fulfilled because we can show the exact equality

$$F_2/2\pi = \frac{1}{2} \int_0^\infty (f_0'^2 - \chi_0'^2 - \chi_0) = 2p_1 \quad (50)$$

from Eq. (45) (this equality is also exactly fulfilled on the level of the second order Eq. (44) [57]). Our above finding $p_2 = 0$ suggests that the next non-vanishing term is actually smaller than $O(\bar{z}_B^{-1})$. This is in accordance with

speculations in Ref. [19] that the leading non-vanishing correction in Eq. (49) is smaller than $O(\bar{z}^1)$. Using Eq. (48), we also obtain the relation $F_2 = 3\pi J_0/2$, which shows that the force-indentation relation at $p = 0$ from Ref. [19], $\bar{F} = F_2 \bar{z}^{1/2} + O(1)$, is exactly identical to the force-indentation relation that has been obtained before in Refs. [21, 58].

C. Energy barrier and force-indentation relation

We can use the exact result (12), where we insert the ansatz (36) to find the leading-order result for the energy barrier, which turns out to be of order $O(\bar{z}_B^{3/2}) = O((p/p_c)\bar{z}_B^2)$,

$$\begin{aligned}\bar{E}_B &= -\frac{1}{4} \int_0^\infty d\rho \bar{\psi}(\partial_\rho \bar{w})^2 \\ &= -\frac{p}{p_c} \bar{z}_B^2 - \frac{1}{2} \bar{z}_B^{3/2} \int_0^\infty dx \chi_0 (2 - 2f_0 + f_0^2) + O(\bar{z}_B^1) \\ &= \frac{p_1}{3} \bar{z}_B^{3/2} + O(\bar{z}_B^1)\end{aligned}$$

with $p_1/3 \simeq 0.27793199$, which leads to Eqs. (33d) and (33e). To show the last equality we use $p_0 = 0$ in the expansion of p , the first integral (40) for $p_0 = 0$, and the last equality in (45). Our numerics show that the next non-vanishing terms in Eqs. (33d) and (33e) are actually $O(\bar{z}_B^{1/2})$ rather than $O(\bar{z}_B)$ and $O((p/p_c)^{-1})$ rather than $O((p/p_c)^{-2})$, respectively. It is not possible to establish this result analytically [analogously to $p_2 = 0$, see Eq. (47)] from symmetry considerations only. Evkin *et al.* find $\bar{E}_B \approx (3/16)^3 J_0^4 (p/p_c)^{-3}$ [21] (see also Table I in Appendix C), which agrees with our result (33e) including the identical numerical prefactor $(3/16)^3 J_0^4 = p_1^4/3$ [see Eq. (48)]. Again, our result for the energy barrier is also consistent with the result (49) of Gomez *et al.* for the indentation energy if it is independent of pressure p [apart from terms of order $(p/p_c)^2$] because

$$\bar{E}_B = \bar{E}_{\text{ind}, p=0}(\bar{z}_B) + \overline{\Delta V}(\bar{z}_B) = \frac{F_2}{12\pi} \bar{z}_B^{3/2}$$

is exactly our above result for $p_1 = F_2/4\pi$; see Eq. (50).

We conclude that the total indentation energy landscape is given by $\bar{E}_{\text{ind}}(\bar{z}) = \bar{E}_{\text{ind}, p=0}(\bar{z}) + \overline{\Delta V}(\bar{z})$ in the Pogorelov limit $\bar{z} \gg 1$, which confirms Eq. (34). Differentiating the energy landscape gives the force-indentation relation $\bar{F}(\bar{z})/2\pi = d\bar{E}_{\text{ind}}/d\bar{z}$ in the presence of a pressure p ,

$$\frac{\bar{F}(\bar{z})}{2\pi} = 2p_1 \bar{z}^{1/2} - 2\frac{p}{p_c} \bar{z}. \quad (51)$$

This generalizes the $p = 0$ result of Ref. [19] and is valid for $\bar{z} \gg 1$ and $p \ll p_c$. It is also identical with the force-indentation relation in the presence of pressure which was conjectured in Ref. [21], tacitly assuming that the Pogorelov dimple energy is independent of the pressure

p . We can now also obtain the maximal force needed to overcome the buckling barrier,

$$\frac{\bar{F}_{\text{max}}}{2\pi} = \frac{1}{2} p_1^2 (p/p_c)^{-2} = \frac{3}{2} \frac{\bar{E}_B}{\bar{z}_B},$$

which is the characteristic maximal point force for structural stability below p_c .

VI. SHALLOW SHELL THEORY FOR THE SHALLOW BARRIER STATE CLOSE TO THE BUCKLING PRESSURE

In this section, we derive several analytical results for the buckling energy landscape for p close to p_c . The total indentation energy landscape is

$$\bar{E}_{\text{ind}} = \frac{\sqrt{2}}{\pi} (1 - p/p_c)^{1/2} \bar{z}^2 - \frac{\sqrt{3}}{4\pi} \bar{z}^3 + O(\bar{z}^4) \quad (52)$$

for shallow indentations with $\bar{z} \ll 1$. By maximizing with respect to \bar{z} at $\bar{F} = 0$, we obtain several analytical results for the energy barrier state for p close to p_c corresponding to shallow barrier states with $\bar{z}_B \ll 1$:

$$\bar{z}_B = \frac{8\sqrt{2}}{3\sqrt{3}} (1 - p/p_c)^{1/2} + O(1 - p/p_c), \quad (53a)$$

$$\overline{\Delta V}_B \approx \frac{4}{3\sqrt{3}} \bar{z}_B \approx \frac{32\sqrt{2}}{27} (1 - p/p_c)^{1/2}, \quad (53b)$$

$$\rho_B \approx \left(\frac{8}{3\sqrt{3}\pi} \right)^{1/2} \simeq 0.70, \quad (53c)$$

$$\bar{E}_B = \frac{\sqrt{3}}{8\pi} \bar{z}_B^3 + O(\bar{z}_B^4), \quad (53d)$$

$$\bar{E}_B = \frac{128\sqrt{2}}{81\pi} (1 - p/p_c)^{3/2} + O((1 - p/p_c)^2). \quad (53e)$$

Thus, we can derive all critical properties of the buckling transition, i.e., all relevant scaling exponents for barrier indentation and barrier energy close to the bifurcation in accordance with the numerical results [see Eqs. (25), (26), (27), (28), (31), and (32)] from nonlinear shallow shell theory. Energy barrier height and barrier indentation vanish as $\bar{E}_B \propto (1 - p/p_c)^{3/2}$ and $\bar{z}_B \propto (1 - p/p_c)^{1/2}$, respectively, which gives rise to softening of the shell close to p_c . We also obtain exact numerical prefactors, which accurately agree with the asymptotic numerical results as Figs. 5, 6, and 7 show.

For p close to p_c the barrier state is a very shallow dimple with $\bar{z}_B \ll 1$, and we can expand about the linear solution (18a) and (18c),

$$\begin{aligned}\bar{w}(\rho) &= \bar{z} \bar{w}_{\text{lin},0} + \bar{z}^2 \bar{w}_1 + \dots, \\ \bar{\psi}(\rho) &= \bar{z} \bar{\psi}_{\text{lin},0} + \bar{z}^2 \bar{\psi}_1 + \dots, \\ \frac{\bar{F}}{2\pi} &= \bar{z} F_0 + \bar{z}^2 F_1 + \dots,\end{aligned} \quad (54)$$

where we define $\bar{w}_{\text{lin},0} \equiv \bar{w}_{\text{lin}}/\bar{z}$ and $\bar{\psi}_{\text{lin},0} \equiv \bar{\psi}_{\text{lin}}/\bar{z}$ as normalized linear displacement and stress function. As \bar{w}_{lin} and $\bar{\psi}_{\text{lin}}$ from Eqs. (18a) and (18c) fulfill the correct boundary conditions, \bar{w}_1 , \bar{w}'_1 , $\bar{\psi}_1$, and $\bar{\psi}'_1$ must vanish at $\rho = 0$ and $\rho \rightarrow \infty$. We note that we perform an expansion for the full problem with $p \neq 0$ close to p_c and also $\bar{F} \neq 0$; i.e., we do not only aim at the $\bar{F} = 0$ barrier state as for the Pogorelov limit in the previous section.

A. Leading order

We insert the expansion (54) into the Eq. (10) for \bar{w} and the compatibility condition (8) for $\bar{\psi}$. To leading linear order \bar{z} the expansion (54) gives the linearized solutions by construction, which motivates the form of the linear term in the expansion (54). They fulfill an inhomogeneous linear differential equation, which is equivalent to the Reissner equations (17),

$$\hat{M} \begin{pmatrix} \bar{w}'_{\text{lin},0} \\ \bar{\psi}'_{\text{lin},0} \end{pmatrix} + \begin{pmatrix} 2(1-p/p_c)\bar{w}'_{\text{lin},0} \\ 0 \end{pmatrix} = \begin{pmatrix} F_0 \\ 0 \end{pmatrix} \quad \text{with} \\ \hat{M} \begin{pmatrix} a \\ b \end{pmatrix} \equiv \begin{pmatrix} \frac{1}{\rho}a - a' - \rho a'' - \rho b - 2\rho a \\ -\frac{1}{\rho}b + b' + \rho b'' - \rho a \end{pmatrix}. \quad (55)$$

We wrote these equations using a linear operator \hat{M} which is self-adjoint with respect to the scalar product $\langle (a, b), (c, d) \rangle \equiv \int_0^\infty d\rho (a(\rho)c(\rho) + b(\rho)d(\rho))$.

We will perform the expansion (54) by employing the linearized solutions in the limit $p \rightarrow p_c$, where

$$\bar{w}_0 \equiv \lim_{p \rightarrow p_c} \bar{w}_{\text{lin},0} = -J_0(\rho), \quad (56) \\ \bar{\psi}_0 \equiv \lim_{p \rightarrow p_c} \bar{\psi}_{\text{lin},0} = -J_1(\rho) = -\bar{w}'_0$$

[see Eqs. (23) and (24)]. The functions \bar{w}'_0 and $\bar{\psi}_0$ provide a solution of the linearized problem at $p = p_c$ where also $\bar{F} = 0$ [because the stiffness vanishes for $p = p_c$ as shown in Sec. III, see (19)]:

$$\hat{M} \begin{pmatrix} \bar{w}'_0 \\ \bar{\psi}_0 \end{pmatrix} = 0. \quad (57)$$

We can use this homogeneous solution to obtain a Fredholm solvability condition for the inhomogeneous problem (55) by scalar multiplication with $(\bar{w}'_0, \bar{\psi}_0)$ on both sides resulting in

$$2(1-p/p_c) \int_0^\infty d\rho \rho \bar{w}'_0 \bar{w}'_{\text{lin},0} = F_0 \int_0^\infty d\rho \bar{w}'_0.$$

Using

$$\int_0^\infty d\rho \bar{w}'_0 = 1, \quad (58)$$

$$\int_0^\infty d\rho \rho \bar{w}'_0 \bar{w}'_{\text{lin},0} \approx \frac{\sqrt{2}}{\pi} (1-p/p_c)^{-1/2} \quad (59)$$

[where the last integral is performed in the limit $p \rightarrow p_c$, see also Eq. (29)], we rediscover our above result (21) for the linear stiffness of the shell,

$$\bar{k} = \lim_{\bar{z} \rightarrow 0} \frac{\bar{F}}{\bar{z}} = 2\pi F_0 = 4\sqrt{2}(1-p/p_c)^{1/2}.$$

B. First order

In the next order \bar{z}^2 , we obtain the inhomogeneous equation

$$\hat{M} \begin{pmatrix} \bar{w}'_1 \\ \bar{\psi}'_1 \end{pmatrix} + \begin{pmatrix} 2(1-p/p_c)\bar{w}'_1 \\ 0 \end{pmatrix} = \begin{pmatrix} -\bar{\psi}_{\text{lin},0}\bar{w}'_{\text{lin},0} + F_1 \\ -\frac{1}{2}\bar{w}'_{\text{lin},0} \end{pmatrix}.$$

Because F_1 will not vanish in the limit $p \rightarrow p_c$, we can perform this limit explicitly and obtain

$$\hat{M} \begin{pmatrix} \bar{w}'_1 \\ \bar{\psi}'_1 \end{pmatrix} = \begin{pmatrix} -\bar{\psi}_0\bar{w}'_0 + F_1 \\ -\frac{1}{2}\bar{w}'_0{}^2 \end{pmatrix}. \quad (60)$$

Again, we use the homogeneous solution (57) to obtain a Fredholm solvability condition by scalar multiplication with $(\bar{w}'_0, \bar{\psi}_0)$ on both sides. This gives [using again the integral (58)]

$$0 = -\frac{3}{2} \int_0^\infty d\rho \bar{\psi}_0 \bar{w}'_0{}^2 + F_1 = \frac{3}{2} \int_0^\infty d\rho J_1^3(\rho) + F_1. \quad (61)$$

Evaluating the last integral, we finally obtain

$$F_1 = -\frac{3\sqrt{3}}{4\pi}.$$

C. Energy barrier and force-indentation relation

From our results for F_0 and F_1 , we find the force-indentation relation

$$\frac{\bar{F}(\bar{z})}{2\pi} = \frac{2\sqrt{2}}{\pi} (1-p/p_c)^{1/2} \bar{z} - \frac{3\sqrt{3}}{4\pi} \bar{z}^2 + O(\bar{z}^3) \quad (62)$$

in the presence of pressure p for shallow dimples $\bar{z} \ll 1$ and for p close to p_c . The force-indentation relation is related by $\bar{F}(\bar{z})/2\pi = d\bar{E}_{\text{ind}}/d\bar{z}$ to the indentation energy landscape. As opposed to the Pogorelov limit $\bar{z} \gg 1$ and $p \ll p_c$ [see Eq. (34)], the pressure does not only enter via the mechanical work term $\bar{p}\Delta\bar{V}(\bar{z})$ for shallow dimples. $[\bar{p}\Delta\bar{V} = (2/\pi)(p/p_c)\Delta\bar{V} \propto -(p/p_c)\bar{z}$ would result in a constant contribution in the force-indentation relation (62)]. For shallow dimples close to p_c , the softening of the shell profoundly modifies the indentation energy already in leading order. Structural stability is governed by the maximal force needed to overcome the barrier,

$$\frac{\bar{F}_{\text{max}}}{2\pi} = \frac{8}{3\sqrt{3}\pi} (1-p/p_c) = \frac{3}{2} \frac{\bar{E}_B}{\bar{z}_B}, \quad (63)$$

which becomes small close to p_c , reflecting the softening of the shell.

For $\bar{F} = 0$, we obtain the relation between pressure and indentation in the post-buckling barrier state (53a), which can also be written as

$$p/p_c = 1 - \frac{27}{128} \bar{z}_B^2. \quad (64)$$

This is the same asymptotic form as found by Evkin *et al.* [21]. Based on the incorrect assumption of zero curvature at the pole in the barrier state [as the normal displacement profiles in Fig. 4(a) clearly show] they find $p/p_c \simeq 1 - 0.048 \bar{z}_B^2$ with a numerical prefactor that differs significantly from our result $27/128 \simeq 0.211$. This leads to significant deviations of their Padé interpolation of p/p_c from the numerical data [see Fig. 5(a)], whereas Eq. (64) is in excellent agreement with the numerics over several decades of the small parameter $1 - p/p_c$ (see Fig. 5). An early result of Thompson for axisymmetric post-buckling shapes (in the absence of a point force) does not agree and features a linear term $O(\bar{z}_B)$ [13, 59].

Integrating $\bar{E}_{\text{ind}} = \frac{1}{2\pi} \int_0^{\bar{z}} \bar{F}(\tilde{z}) d\tilde{z}$, we find the total indentation energy landscape (52) and all results for the energy barrier state. The energy barrier can also be calculated directly from the exact result (12), where we obtain in leading order

$$\begin{aligned} \bar{E}_B &= -\frac{1}{4} \int_0^\infty d\rho \bar{\psi} \bar{w}'^2 \\ &\approx -\bar{z}^3 \frac{1}{4} \int_0^\infty d\rho \bar{\psi}_0 \bar{w}_0'^2 = \bar{z}_B^3 \frac{1}{4} \int_0^\infty d\rho J_1^3(\rho) = \frac{\sqrt{3}}{8\pi} \bar{z}_B^3, \end{aligned}$$

in agreement with (53d). The indentation volume (53b) at the barrier state is found by using the barrier indentation (53a) in the exact relation (11) or relation (29).

VII. ENERGY LANDSCAPE AND BARRIER

A. Energy landscape

Both in the Pogorelov limit and the softening limit close to p_c , we obtained the exact asymptotics of the full energy landscape, (34) and (52), which also contains all information about the energy barrier [by maximizing $\bar{E}_{\text{ind}}(\bar{z})$ with respect to \bar{z}] and the force-indentation curves $\bar{F}(\bar{z})/2\pi = d\bar{E}_{\text{ind}}/d\bar{z}$. Both limits can be written in a scaling form

$$\bar{E}_{\text{ind}} = \bar{E}_B f\left(\frac{\bar{z}}{\bar{z}_B}\right), \quad (65)$$

$$\frac{\bar{F}(\bar{z})}{2\pi} = \frac{\bar{E}_B}{\bar{z}_B} f'\left(\frac{\bar{z}}{\bar{z}_B}\right) \quad (66)$$

with two characteristic scaling functions

$$\begin{aligned} f_{\text{Pog}}(z) &= 4z^{3/2} - 3z^2, \\ f_{\text{soft}}(z) &= 3z^2 - 2z^3 \end{aligned} \quad (67)$$

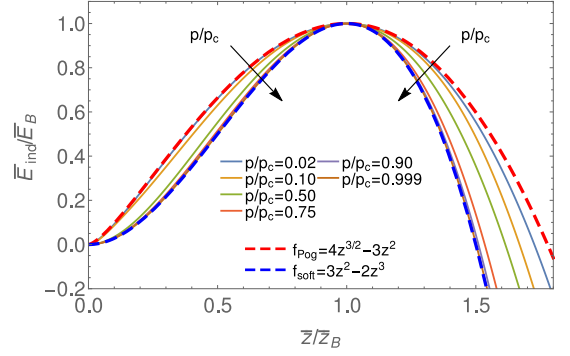


FIG. 10. Solid lines: Numerical results for the rescaled energy landscape $\bar{E}_{\text{ind}}/\bar{E}_B$ as a function of rescaled indentation $z \equiv \bar{z}/\bar{z}_B$ for various pressures p/p_c according to Eq. (65). Arrows indicate increasing pressure. All rescaled landscapes lie between the two limiting scaling curves $f_{\text{Pog}}(z)$ and $f_{\text{soft}}(z)$, which are known analytically [dashed lines; see Eq. (67)] and approached for $p/p_c \ll 1$ or p/p_c close to unity, respectively.

determining the shape of the energy landscape, which is in good agreement with our numerical results in Fig. 10. We note that the Pogorelov result applies for $\bar{z} \gg 1$ and $p \ll p_c$, whereas the softening regime applies to $\bar{z} \ll 1$ and p close to p_c . In particular, it is not possible to calculate the linear shell stiffness $k = d^2 \bar{E}_{\text{ind}}/d\bar{z}^2|_{\bar{z}=0}$ from the Pogorelov result for $p \ll p_c$. For this, one has to resort to the linear response result (21) as has been discussed in Ref. [52].

B. Volume and area change during indentation

During point force indentation, area and volume change according to Eqs. (13) and (14). According to relation (15), the indentation area change is given by the force-indentation relation via $\Delta \bar{A}(\bar{z}) = -2\bar{F}(\bar{z})$. The above scaling relation (66) for the force-indentation relation is in good agreement with our numerical results for the area change, as Fig. 11(a) shows. The area change is a non-monotonous function of \bar{z} with a minimum at the maximal point force $-\bar{F}_{\text{max}} = \frac{1}{2} \Delta \bar{A}_{\text{min}}$.

In the linear response regime $\bar{z} \ll 1$, also the volume change $\Delta \bar{V}(\bar{z})$ is given by the point force via $\Delta \bar{V}(\bar{z}) = 2\pi \int_0^\infty d\rho \rho \bar{w}_{\text{lin}} = -\bar{k}(p)\bar{z} = -\bar{F}$; see Eqs. (19) and (21). For deeper indentations, we can use the results (29) close to p_c and the mirror-inverted dimple result $\Delta \bar{V} = -\pi \bar{z}^2/2$ to find

$$-\Delta \bar{V}(\bar{z}) \approx \begin{cases} \bar{k}(p)\bar{z} + \frac{\bar{z}^2}{2\sqrt{2}} (1 - p/p_c)^{-1/2} & \text{for } p \approx p_c \\ \bar{k}(p)\bar{z} + \pi \bar{z}^2/2 & \text{for } p \ll p_c \end{cases}. \quad (68)$$

Rescaling with the barrier indentation \bar{z}_B [see Eqs. (53a) and (33a)] and the indentation volume $\Delta \bar{V}_B$ at the barrier [see Eqs. (53b) and (33b)], we find that both for

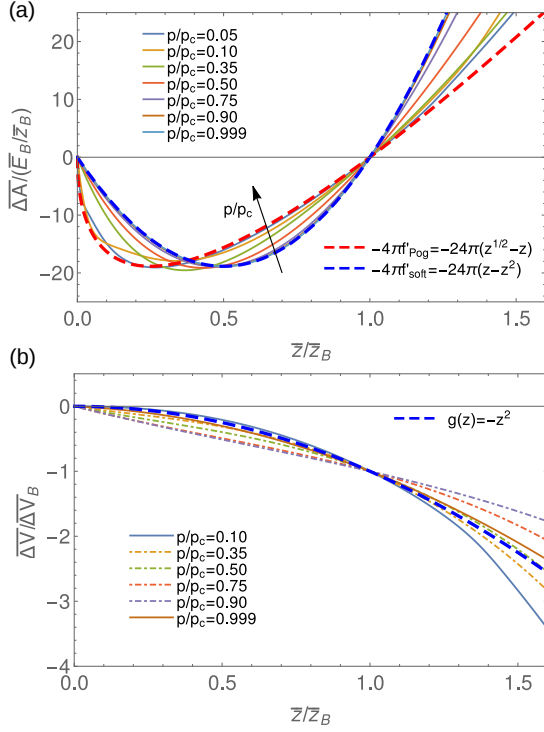


FIG. 11. Numerical results for (a) the rescaled area $\overline{\Delta A}/(\overline{E}_B/\overline{z}_B)$ and (b) rescaled volume $\overline{\Delta V}/\overline{\Delta V}_B$ change as a function of $z \equiv \overline{z}/\overline{z}_B$ for various pressures p/p_c according to Eqs. (66) and (69). The dashed lines indicated the limiting scaling functions according to Eqs. (67) and (69).

$p \approx p_c$ and $p \ll p_c$ a scaling relation

$$-\overline{\Delta V}(\overline{z}) = \overline{\Delta V}_B g\left(\frac{\overline{z}}{\overline{z}_B}\right) \quad (69)$$

with $g(z) = \pi \overline{z}^2/2$ (70)

holds over a wide range $\overline{z}/\overline{z}_B \gg (1 - p/p_c)^{1/2}$ and $\overline{z}/\overline{z}_B \gg (p/p_c)^2$, respectively. For intermediate pressures, however, an additional linear regime emerges; see Fig. 11(b). Volume and area change during point force indentation combine to a reduced volume

$$v = V/(4\pi/3)(A/4\pi)^{3/2} = \frac{1 + \gamma^{-1} \frac{3}{4\pi} \overline{\Delta V}}{(1 + \gamma^{-1} \frac{1}{2\pi} \overline{\Delta A})^{3/2}} < 1, \quad (71)$$

which is monotonously decreasing and reduced to $v = 1 - O(\gamma^{-1})$ up to the barrier. It becomes significantly reduced and finally vanishes only close to the snap through where $z \propto R_0$ or $\overline{\Delta V} \propto \overline{z}^2 \propto \gamma$.

C. Quantitative interpolation for energy barrier and indentation

The scaling forms (65) and (66) give quantitatively accurate energy barrier shapes and force-indentation relations if accurate interpolation results for the energy barrier height \overline{E}_B and the barrier indentation \overline{z}_B are available. As non-dimensionalization of the shallow shell Eqs. (7) and (8) showed, the dimensionless energy barrier \overline{E}_B at $\overline{F} = 0$ can only depend on p/p_c ,

$$\overline{E}_B = f_p(p/p_c). \quad (72)$$

Based on our analytic asymptotic results (33e) and (53e) for the function $f_p(x)$, we can give a new interpolation formula, significantly improving the interpolation formula for the function $f_p(x)$ proposed in Ref. [9] (which was based on scaling results in the Pogorelov limit and numerical results only):

$$f_p(x) = \left(a_3 x^{-3} + a_2 x^{-2} + a_1 x^{-1} + a_0 + \left(1 - \sum_{n=0}^3 a_n\right) x \right) \times \left[b_{3/2} (1-x)^{3/2} + b_2 (1-x)^2 + (1 - b_{3/2} - b_2) (1-x)^{5/2} \right],$$

$$a_3 = \frac{p_1^4}{3} \simeq 0.161, \quad a_2 = -0.0168,$$

$$a_1 = 1.653, \quad a_0 = 1.951,$$

$$b_{3/2} = \frac{128\sqrt{2}}{81\pi} \simeq 0.711, \quad b_2 = 3.794. \quad (73)$$

Our analytical asymptotic results constrain the values a_3 and $b_{3/2}$. The remaining fit parameters are determined by a Levenberg-Marquardt fit on numerical shallow shell data for the energy barrier that are equally distributed between $p = 0$ and $p = 1$ in steps of $\Delta p = 0.01$. The fact that the fit gives $|a_2| \ll 1$ is consistent with our numerical finding that the next non-vanishing term in Eq. (33e) is actually $O((p/p_c)^{-1})$ rather than $O((p/p_c)^{-2})$. Relative deviations from the numerical shallow shell data are smaller than 5% for $p/p_c < 0.6$ and smaller than 20% over the whole range of p ; see Fig. 8.

A similar interpolation can be given for the barrier indentation:

$$\overline{z}_B = g_p(p/p_c) \quad \text{with}$$

$$g_p(x) = \left(a_2 x^{-2} + a_0 + a_{-1} x + \left(1 - \sum_{n=-1}^2 a_n\right) x^2 \right) \times \left[b_{1/2} (1-x)^{1/2} + b_1 (1-x) + (1 - b_{1/2} - b_1) (1-x)^{3/2} \right],$$

$$a_2 = p_1^2 \simeq 0.695, \quad a_0 = 4.779, \quad a_{-1} = -3.144,$$

$$b_{1/2} = \frac{8\sqrt{2}}{3\sqrt{3}} \simeq 2.177, \quad b_1 = -1.377, \quad (74)$$

see Fig. 5, where our analytical results constrain the values a_2 , $b_{1/2}$, and $a_1 = 0$ [the leading non-vanishing correction in the Pogorelov limit is $O((p/p_c)^0)$ because of $p_2 = 0$; see Eqs. (47) and (33a)]. Relative deviations from the numerical results are smaller than 2% for $p/p_c < 0.6$ and smaller than 15% over the whole range of p .

We can also employ the strategy of Evkin *et al.* [21] and use a Padé interpolation of p/p_c as a function of \bar{z}_B . With an ansatz

$$\frac{p}{p_c} = \frac{\sum_{n=0}^4 \alpha_n \varepsilon^n}{1 + \sum_{n=1}^4 \beta_n \varepsilon^n} \quad \text{with } \varepsilon \equiv 2\bar{z}_B^{-1/2}, \quad (75)$$

we can incorporate the analytical constraints $\alpha_0 = 0$, $\alpha_1 = p_1/2 \simeq 0.417$ from the Pogorelov limit $\varepsilon \ll 1$ with (46) and constraints $\alpha_n = \beta_n$ for $n = 1, 2, 3, 4$ and $\alpha_4 = 8/27 \simeq 0.296$ from the shallow dimple regime $\varepsilon \gg 1$ with (64). Furthermore, the constraint $p_2 = 0$ from the Pogorelov limit $\varepsilon \ll 1$ [see Eq. (47)] gives $\alpha_2 = p_1^2/4 \simeq 0.174$. The only unconstrained coefficient α_3 can be used for a Levenberg-Marquardt fit of the numerical shallow shell data, which gives $\alpha_3 \simeq 0.476$. Our Padé interpolation of p/p_c differs significantly from the one given in Ref. [21] because of the corrected behavior in the limit $p \approx p_c$ [see Fig. 5(a)]; relative deviations from the numerical results for p/p_c are smaller than 5% over the whole range of z_B .

VIII. MAXWELL AND UNBUCKLING PRESSURE

We can use the energy landscape (34) in the Pogorelov limit $\bar{z} \gg 1$ to calculate the critical unbuckling pressure p_{cu} and the Maxwell pressure p_{c1} . When we reduce the compressive pressure to $p < p_{cu} < p_c$, the buckled state can no longer be stabilized, and both the buckled state and the unstable barrier transition state merge and vanish in a saddle-node bifurcation at $p = p_{cu}$. The unbuckling pressure is the smallest compressive pressure at which a metastable buckled state still exists and is thus also called minimum buckling load [5, 14, 48, 60]. The stable buckled states assumed after buckling at p_c are snap-through buckled states ($z \approx 2R_0$) and can no longer be described in shallow shell approximation, which assumes small slopes $|w'| \sim z/R_0 \ll 1$, i.e., small rotation angles of shell elements. By numerical solution of the full shape equations [3], which are valid beyond the shallow shell approximation, we find that at unbuckling at the pressure p_{cu} the shell is no longer fully snapped-through but the indentation is still deep and proportional to R_0 , i.e., $z = \alpha R_0$ with $\alpha \sim 1.4 - 1.5$ (in agreement with Refs. [5, 60]).

If we assume that also the unbuckling state has maximal indentation $z = 2R_0$ or $\bar{z} = 2\gamma^{1/2}$ with $\bar{z} \gg 1$ for thin shells $R_0 \gg h$ or large Föppl-von Kármán numbers $\gamma \gg 1$, this state can only be a boundary minimum of the energy landscape (34) with $\bar{F} = 0$ if the maximum

of the energy landscape at z_B has smaller indentation $z_B < 2R_0$ or $\bar{z}_B < 2\gamma^{1/2}$. This is the case above the critical unbuckling pressure

$$p_{cu} = \frac{p_1}{\sqrt{2}} p_c \gamma^{-1/4}. \quad (76)$$

For $p < p_{cu}$, the precompressed spherical state is the *only* accessible energy minimum and, thus, spherical shells have to unbuckle. The parameter dependence $p_{cu} \propto p_c \gamma^{-1/4}$ has been previously observed [5, 16, 47, 60]. In Refs. [5, 60], $p_{cu} \simeq 2.65 p_c \gamma^{-1/4}$ has been found using a shell theory that allows for large deflections and rotation angles. Solving the full shape equations from Ref. [3] numerically we find $p_{cu} \simeq 1.2 p_c \gamma^{-1/4}$, which is by a factor of 2 larger than the shallow shell result (76) but also shows the same parameter dependence. We conclude that in shallow shell theory the unbuckling state is not properly accessible but can be approximately regarded as a boundary minimum at $z = 2R_0$ corresponding to a snap-through state. The simple condition $z_B = 2R_0$ for the barrier state can predict the unbuckling pressure p_{cu} up to a numerical factor of about 2.

We can calculate the Maxwell pressure p_{c1} , at which the snap-through buckled state and the unbuckled precompressed spherical state have equal energies, from calculating the zero $\bar{E}_{ind}(\bar{z}_1) = 0$ of the energy landscape (34) (see also Fig. 2)

$$\bar{z}_1 = \frac{16p_1^2}{9} (p/p_c)^{-2} = \frac{16}{9} \bar{z}_B. \quad (77)$$

The buckled state with equal energy is the snap-through state if $z_1 = 2R_0$ or $\bar{z}_1 = 2\gamma^{1/2}$. This condition determines the Maxwell pressure

$$p_{c1} = \frac{4p_1}{3\sqrt{2}} p_c \gamma^{-1/4} = \frac{4}{3} p_{cu}, \quad (78)$$

confirming the parameter dependence $p_{c1} \sim p_c \gamma^{-1/4}$ [17]. Using the Pogorelov theory $p_{c1} \simeq 0.901(1 - \nu^2)^{-1/4} p_c \gamma^{-1/4}$ has been obtained [47], which slightly deviates from our above result $p_{c1} \simeq 0.786 p_c \gamma^{-1/4}$ from shallow shell theory. The relation $p_{c1} = 4p_{cu}/3$ is obtained identically using Pogorelov theory [47].

IX. SOFT SPOTS

The critical unbuckling pressure can be interpreted as a finite-size effect that leads to spontaneous unbuckling if the critical indentation at the barrier does no longer “fits” into the capsule in normal direction, i.e., if $z_B > 2R_0$ or $\bar{z}_B > 2\gamma^{1/2}$. Because $\rho_B \propto \bar{z}_B^{1/2} \ll \bar{z}_B$ for mirror-inverted dimples the lateral extent ρ_B of the critical barrier state does not conflict with the finite size R_0 of the shell. This can happen, however, for spherical caps under pressure [61] or soft spots on a sphere under pressure [16] if their lateral size L (or opening angle $\alpha = L/R_0$ for a spherical cap) are small. Then the finite lateral size L can trigger

unbuckling of the cap or the soft spot. The important parameter governing the buckling of a finite spherical cap is $\lambda \equiv L/l_{\text{el}} = \bar{L}$ [16, 61]. Although the boundary conditions play an important role and differ from those of a complete spherical shell both for clamped and free caps or soft spots, we expect that unbuckling is triggered if $\lambda = \bar{L} < \rho_B(p)$ because a fully buckled state of extent \bar{L} becomes an unstable boundary energy maximum then. According to Eqs. (33c) and (53c), it will unbuckle if $p/p_c < p_1/\bar{L}$ for $\bar{L} \gg 1$ and for *all* $\bar{L} < 0.70$ for p close to p_c . Therefore, soft spots sufficiently small compared to the the elastic length ($L < 0.70l_{\text{el}}$) will immediately unbuckle for p smaller than p_c . This will suppress the existence of the subcritical barrier state and hysteresis in the buckling of sufficiently small soft spots: The soft spot buckles *and* unbuckles at the same threshold pressure p_c .

X. BIFURCATION BEHAVIOR AS A FUNCTION OF PRESSURE

Our results on the buckling barrier of a perfect spherical shell allow us to classify the buckling bifurcation as a function of the control parameter p in more detail, as schematically shown in Fig. 12. A suitable order parameter to trace the bifurcation is the indentation z . The functional form of the energy landscape (52) close to p_c (containing z^2 - and z^3 -terms) suggests a transcritical bifurcation at $p = p_c$, but the unstable barrier state does not continue as a stable equilibrium state into the buckled phase $p > p_c$, where Eq. (52) is no longer applicable. Clearly, the bifurcation at $p = p_c$ is subcritical as the barrier states represent a subcritical branch of unstable stationary points, which are already present for $p < p_c$ (and $p > p_{\text{cu}}$). From this fixed point structure with an unstable barrier state with $\bar{z}_B \propto (1 - p/p_c)^{1/2}$ [Eq. (53a)] and the stable spherical state joining at $p = p_c$ and resulting in an unstable spherical state for $p > p_c$, the bifurcation at $p = p_c$ is similar to a subcritical pitchfork, in which the spherical state $z = 0$ becomes unstable. We have, however, only a “one-sided” pitchfork because we only consider compressed states $z < 0$ and there is no inversion symmetry $z \rightarrow -z$ between compression and deflation of a sphere. The buckled snap-through state $z = 2R_0$ is stabilized as a boundary minimum for $p > p_{\text{cu}}$ and becomes the only remaining minimum after the bifurcation at $p = p_c$. It becomes the global energy minimum at the Maxwell pressure p_{c1} between p_{cu} and p_c . The appearance of the buckled state together with the energy barrier state at $p = p_{\text{cu}}$ is a saddle-node or fold bifurcation as results in Refs. [3, 17, 60] suggest. For pressures slightly above p_{cu} the buckled state snaps through. Bifurcations at p_c and p_{cu} result in hysteresis for $p_{\text{cu}} < p < p_c$ between saddle-node and subcritical bifurcation. Upon approaching the buckling instability from $p < p_c$, the shell indentation at the energy barrier maximum vanishes $\propto (1 - p/p_c)^{1/2}$ and the linear restoring force vanishes as the linear stiffness $\propto (1 - p/p_c)^{1/2}$;

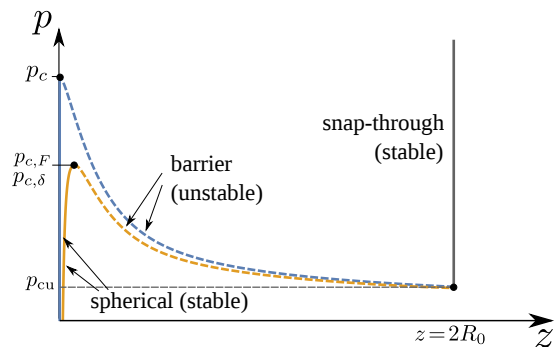


FIG. 12. Bifurcation behavior of the indentation z with pressure p as control parameter for a perfect shell (blue) or in the presence of a preindenting force or for an imperfect shell (yellow) in shallow shell theory. There are three types of stationary states: a stable spherical state for $p < p_c$ (or $p < p_{c,F}$, $p < p_{c,\delta}$) (solid lines), an unstable barrier state corresponding to an energy maximum (dashed lines), and a stable snap-through state above the unbuckling pressure $p > p_{\text{cu}}$ (solid gray line). In shallow shell theory, the unbuckling and snap-through states are not properly accessible but can be regarded as boundary minimum at $z = 2R_0$.

see also Eq. (62). Right at the instability, the linear restoring force vanishes and the force-indentation curve $\bar{F} \propto -\bar{z}^2$ misses linear terms such that we can also expect a “critical slowing down” of the buckling dynamics [62].

XI. BIFURCATION BEHAVIOUR AND SOFTENING IN THE PRESENCE OF A PREINDENTING POINT FORCE

One view of the point force F is to consider F as a probe of the buckling barrier for a fixed subcritical pressure $p < p_c$, which gives access to the bifurcation behavior as a function of p . An alternative view is to consider the point force as an additional control parameter and consider its effect on the buckling bifurcation, i.e., to consider how the buckling bifurcation as a function of p is modified if the sphere is preloaded by a small point force F_{pre} . Then, F_{pre} acts analogously to an additional ordering field in a phase transition bifurcation favoring one phase (here the buckled state), gives rise to an *avoided* or *perturbed bifurcation* at a reduced critical pressure $p_{c,F} < p_c$, and turns the bifurcation at $p_{c,F}$ into a saddle-node bifurcation (see Fig. 12). The bifurcation at p_{cu} remains essentially unchanged as long as \bar{F}_{pre} is small. Interestingly, imperfections will have a very similar effect as we will show below.

In the presence of a preloading point force $F_{\text{pre}} > 0$, the critical buckling pressure is reduced to $p_{c,F} < p_c$ as it is easier to buckle a preloaded shell. The additional force F_{pre} tilts the energy landscape to $\bar{E}_{\text{ind}} - \bar{F}_{\text{pre}}\bar{z}/2\pi$, resulting in the modified force-indentation relation $\bar{F}(\bar{z}) =$

$2\pi d\bar{E}_{\text{ind}}/d\bar{z} - \bar{F}_{\text{pre}}$. Equivalently, we can say that \bar{F} is replaced by the total force $\bar{F} + \bar{F}_{\text{pre}}$ in the original force-indentation relation. This turns the bifurcation at $p_{c,F}$ into a saddle-node bifurcation, at which both the stationarity condition $\bar{F}_{\text{pre}} = 2\pi d\bar{E}_{\text{ind}}/d\bar{z}$ for the tilted energy landscape (i.e., $\bar{F}(\bar{z}) = 0$ for the modified force-indentation relation) and the saddle condition $0 = d^2\bar{E}_{\text{ind}}/d\bar{z}^2 = d\bar{F}(\bar{z})/d\bar{z}$ have to be fulfilled.

For small forces \bar{F}_{pre} , the bifurcation still occurs close to p_c and for small indentations \bar{z} , such that we can use the asymptotic energy landscape (52) and the force-indentation relation (62). Stationarity and saddle conditions then result in a reduced critical pressure with a knockdown factor

$$\frac{p_{c,F}}{p_c} = 1 - \frac{3\sqrt{3}}{16}\bar{F}_{\text{pre}}. \quad (79)$$

For $p < p_{c,F}$, two stationary states emerge in the saddle-node bifurcation (see Fig. 12): a stable preindented spherical state and the unstable barrier state. The stable preindented state is no longer a perfect precompressed sphere with $\bar{z} = 0$ but has a finite indentation $\bar{z}_{\text{sph}} \approx F_{\text{pre}}/k$, which is very well described by the linear stiffness k from Eq. (21). Solving the stationarity condition $\bar{F}_{\text{pre}} = 2\pi d\bar{E}_{\text{ind}}/d\bar{z}$, i.e., solving the force-indentation relation (62) for \bar{z} , we obtain the indentation for both branches,

$$\bar{z}_{B,\text{sph}} = \bar{z}_{+,-} = \frac{4\sqrt{2}}{3\sqrt{3}} \left[\left(1 - \frac{p}{p_c}\right)^{1/2} \pm \left(\frac{p_{c,F} - p}{p_c}\right)^{1/2} \right],$$

which meet for $p = p_{c,F}$ at $z_B = z_{\text{sph}} \sim \sqrt{F_{\text{pre}}}$. Interestingly, we find the same softening behavior as in the absence of the preloading force if the pressure approaches the critical value $p_{c,F}$. The indentation difference from spherical to barrier state is

$$\bar{z}_{B,F} = \bar{z}_B - \bar{z}_{\text{sph}} = \frac{8\sqrt{2}}{3\sqrt{3}} \left(\frac{p_{c,F} - p}{p_c}\right)^{1/2} \quad (80)$$

and the corresponding energy barrier is

$$\begin{aligned} \bar{E}_{B,F} &= \bar{E}_B - \bar{E}_{\text{sph}} = \frac{1}{2\pi} \int_{z_{\text{sph}}}^{\bar{z}_B} \bar{F}(z) dz \\ &= \frac{128\sqrt{2}}{81\pi} \left(\frac{p_{c,F} - p}{p_c}\right)^{3/2} = \frac{\sqrt{3}}{8\pi} \bar{z}_{B,F}^3. \end{aligned} \quad (81)$$

Both results are completely analogous to Eqs. (53a), (53d), and (53e) for $\bar{F}_{\text{pre}} = 0$, with $\Delta\bar{p} \equiv (p_{c,F} - p)/p_c$ replacing $(1 - p/p_c)$. They result in a linear stiffness

$$k_F = \left. \frac{d^2\bar{E}_{B,F}}{d\bar{z}_{B,F}^2} \right|_{\bar{z}_{B,F}=0} = 4\sqrt{2} \left(\frac{p_{c,F} - p}{p_c}\right)^{1/2},$$

giving rise to the same softening behavior close to $p_{c,F}$ as in Eq. (21) in the absence of the preloading force. The

properties of the subcritical barrier such as the scaling $\bar{z}_{B,F} \propto \Delta\bar{p}^{1/2}$ and $\bar{E}_{B,F} \propto \Delta\bar{p}^{3/2}$, which characterize the softening of the shell close to the critical pressure $p_{c,F}$ are *universal* and independent of the applied point force \bar{F}_{pre} . For a saddle-node bifurcation, where two branches of fixed points (\bar{z}_B and \bar{z}_{sph}) smoothly merge at the critical value $p = p_{c,F}$ of the control parameter, the behaviors $\bar{z}_{B,F} \propto \Delta\bar{p}^{1/2}$ and $\bar{E}_{B,F} \propto \Delta\bar{p}^{3/2}$ are actually generic.

Figure 13 shows numerical results for the knockdown factor, the bifurcation of the indentation, the indentation difference, and the energy barrier between barrier state and preindented spherical state. The numerical method is unchanged, in principle. In the presence of a preindenting force, the total force $\bar{F} + \bar{F}_{\text{pre}}$ is acting on the shell, and \bar{F} is replaced by the total force $\bar{F} + \bar{F}_{\text{pre}}$ in the shallow shell equations that are solved numerically. Both at the barrier state and at the preindented spherical state we have an applied force $\bar{F} = 0$, but the total force acting on the shell is not vanishing but equals the preindenting force \bar{F}_{pre} . In order to calculate the barrier energy $\bar{E}_{B,F} = \bar{E}_B - \bar{E}_{\text{sph}}$ directly without numerically integrating the full force-indentation relation, we now employ a generalized version of relation (12), which gives direct numerical access to the energy difference $\Delta\bar{E}_{\text{tot},F}$ between a state indented with a force \bar{F}_{pre} and the precompressed unindented spherical state (with the same pressure but with $\bar{z} = 0$) as

$$\begin{aligned} \Delta\bar{E}_{\text{tot},F} &= -\frac{1}{4} \int_0^\infty d\rho \bar{\psi} (\partial_\rho \bar{w})^2 - \frac{\bar{F}_{\text{pre}}}{4\pi} \bar{z} \\ &\quad - 2(1 + \nu) \frac{p}{p_c} \frac{\bar{F}_{\text{pre}}}{2\pi}. \end{aligned} \quad (82)$$

A derivation is given in Appendix A. The energy barrier $\bar{E}_{B,F} = \Delta\bar{E}_{\text{tot},B} - \bar{E}_{\text{tot},\text{sph}}$ can then be obtained as difference of the values of $\Delta\bar{E}_{\text{tot},F}$ between the barrier state and the preindented spherical state, both of which can be obtained via continuation of solutions of the shallow shell equations (7) and (8) with force \bar{F}_{pre} .

The numerical results in Fig. 13 show that the above results (80) and (81) are quantitatively correct only for very small $\bar{F}_{\text{pre}} \ll 1$, where the knockdown factor (79) is close to unity and we can use the asymptotic result (62) for the force-indentation relation [see inset in Fig. 13(a)]. For larger \bar{F}_{pre} , it turns out that prefactors in Eqs. (80) and (81) depend weakly on the preindentation force \bar{F}_{pre} , and the knockdown factor deviates from Eq. (79).

In order to explain these results quantitatively, we use analytical estimates based on the scaling form (65) of the energy landscape for $\bar{F} = 0$ employed in conjunction with the interpolation formulas (73) and (74) for the pressure dependence of $\bar{E}_{B,0}$ and $\bar{z}_{B,0}$ for $F_{\text{pre}} = 0$. The knockdown factor $p_{c,F}/p_c$ is then determined by the solution of

$$\frac{3}{2} \frac{\bar{E}_{B,0}(p_{c,F}/p_c)}{\bar{z}_{B,0}(p_{c,F}/p_c)} = \frac{\bar{F}_{\text{pre}}}{2\pi} \quad (83)$$

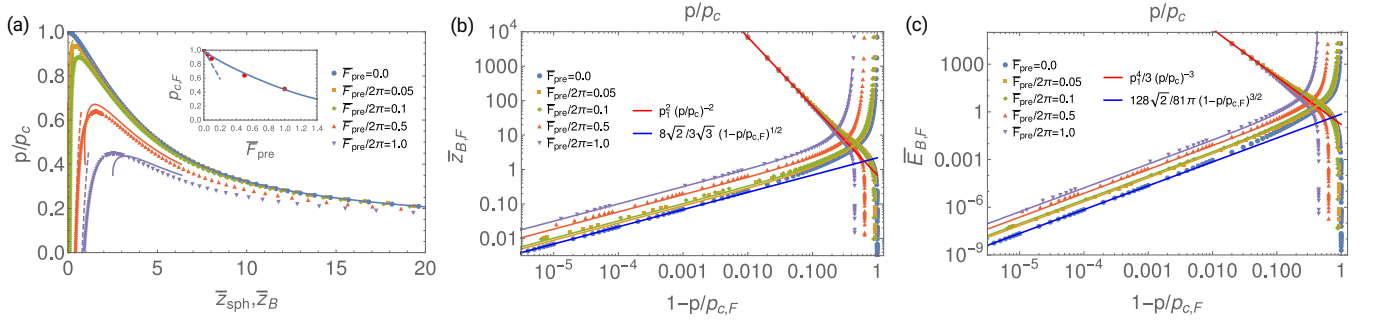


FIG. 13. (a) Bifurcation of the indentation as a function of the pressure for a shell preindented with force \bar{F}_{pre} . Below a critical pressure $p_{c,F}$, two branches of shapes emerge in a saddle-node bifurcation, an indented spherical branch with \bar{z}_{sph} and an unstable barrier state with \bar{z}_B . Dashed lines: Linear response $\bar{z}_{\text{sph}} \approx \bar{F}_{\text{pre}}/k$ of spherical shell. Solid lines: Approximation (84). Inset: Knockdown factor $p_{c,F}/p_c$ as a function of preindenting force \bar{F}_{pre} as compared to Eq. (83) (solid line) and small \bar{F}_{pre} approximation (79) (dashed line). (b) Indentation difference $\bar{z}_{B,F} = \bar{z}_B - \bar{z}_{\text{sph}}$ as a function of pressure p/p_c (upper curves and upper horizontal scale) together with analytical result (33a) for $\bar{F}_{\text{pre}} = 0$ (red line) and as a function of $1 - p/p_{c,F}$ (lower curves and lower horizontal scale) together with analytical result (53a) for $\bar{F}_{\text{pre}} = 0$ (blue line). Lines are approximation (85). (c) Energy barrier $\bar{E}_{B,F}$ as a function of pressure p/p_c (upper curves and upper horizontal scale) together with the analytical result (33e) for $\bar{F}_{\text{pre}} = 0$ (red line) and as a function of $1 - p/p_{c,F}$ (lower curves and lower horizontal scale) together with the analytical result (53e) for $\bar{F}_{\text{pre}} = 0$ (blue line). Lines are approximation (86).

and

$$\bar{z}_{B,\text{sph}} = \frac{1}{2}\bar{z}_{B,0} \left(1 \pm \left(1 - \frac{\bar{F}_{\text{pre}}}{2\pi} \frac{2}{3} \frac{\bar{z}_{B,0}(p)}{\bar{E}_{B,0}(p)} \right)^{1/2} \right), \quad (84)$$

$$\bar{z}_{B,F} = \bar{z}_B - \bar{z}_{\text{sph}} = \bar{z}_{B,0} \left(1 - \frac{\bar{F}_{\text{pre}}}{2\pi} \frac{2}{3} \frac{\bar{z}_{B,0}(p/p_c)}{\bar{E}_{B,0}(p/p_c)} \right)^{1/2}, \quad (85)$$

$$\bar{E}_{B,F} = \bar{E}_{B,0} \left(1 - \frac{\bar{F}_{\text{pre}}}{2\pi} \frac{2}{3} \frac{\bar{z}_{B,0}(p/p_c)}{\bar{E}_{B,0}(p/p_c)} \right)^{3/2}, \quad (86)$$

where we used the scaling function $f_{\text{soft}}(z)$ appropriate for $p/p_c \gtrsim 0.75$. This describes our numerical data for the modified bifurcation behavior in Fig. 13 well for $\bar{F}_{\text{pre}} \lesssim 1$. We recover again the universal properties of the subcritical barrier $\bar{z}_{B,F} \propto \Delta p^{1/2}$ and $\bar{E}_{B,F} \propto \Delta p^{3/2}$, but prefactors in these scaling laws now depend on the applied point force \bar{F}_{pre} .

Effects of the preindenting force F_{pre} are negligible for the barrier state in the Pogorelov limit $\bar{z}_B \gg 1$ and $p \ll p_c$. Then the barrier state is deeply indented, and the preindenting force \bar{F}_{pre} can be neglected versus the elastic and pressure terms in the force-indentation relation (51) for $\bar{z}_B \gg \bar{F}_{\text{pre}}^2$ or $p/p_c \ll 1/\bar{F}_{\text{pre}}$. The linear shell stiffness $\bar{k} = \frac{d\bar{F}}{d\bar{z}}$ [see Eq. (21)], on the other hand, is independent of an additional constant force \bar{F}_{pre} in the force-indentation relation. Thus, the preindented spherical state approaches $\bar{z}_{\text{sph}} \approx \bar{F}_{\text{pre}}/k \simeq 0.8\bar{F}_{\text{pre}}$ for $p/p_c \approx 0$, which is also negligible versus $\bar{z}_B \sim (p/p_c)^{-2}$ for $p/p_c \ll 1/F_{\text{pre}}^{1/2}$. Therefore, the indentation difference from spherical to barrier state $\bar{z}_{B,F} \approx \bar{z}_B$ and the barrier energy $\bar{E}_{B,F} \approx \bar{E}_B$ approach the Pogorelov asymptotics (33a) and (33e) in the Pogorelov limit for $p/p_c \ll 1/F_{\text{pre}}^{1/2}$; see also Fig. 13. Therefore, the bifurca-

tion at $p_{\text{cu}}/p_c \sim \gamma^{-1/4}$ [see Eq. (76)] remains essentially unchanged as long as $\bar{F}_{\text{pre}} \ll \gamma^2$, which is a rather weak condition.

XII. IMPERFECTIONS

For applications, another important class of “quenched” defects are imperfections in form of a normal axisymmetric displacement field $w_I(r)$, which is already present in the strain-free state of the shell [10, 13, 15, 63]. Then the strain is defined relative to the configuration of a sphere with radius $R(r) = R_0 + w_I(r)$ containing already normal displacements $w_I(r)$. Similar to the preindenting force, also imperfections are known to affect the nature of the bifurcation at p_c and cause a pronounced reduction of the critical buckling pressure p_c [13–15]. We will show that the effect of localized axisymmetric imperfections is very similar to the effect of a preindenting force.

A. Shallow shell theory in the presence of imperfections

We consider here axisymmetric imperfections and demonstrate that they can be incorporated in an exact manner into our analytical barrier calculation based on the shallow shell equations in the regime of small $\bar{z}_B \ll 1$ from Sec. VI. A detailed derivation of the nonlinear shallow shell equations in the presence of imperfections is given in Appendix B.

In-plane strains u_{ij} are defined relative to the imperfect initial shape and depend on the imperfection field w_I via nonlinear terms in the normal displacement w .

Changes in the curvature tensor (curvature strains) k_{ij} , on the other hand, are independent of w_I . The Hookean stress-strain relations giving in-plane stresses σ_{ij} and bending moments in terms of the in-plane strains u_{ij} and curvature strains k_{ij} , respectively, are not modified by imperfections, as well as the Hookean elastic energy of the shell in terms of strains [see Eq. (B1) in Appendix B]. Variation with respect to the additional normal displacements $w(r)$ (and in-plane displacements) finally gives the modified shallow shell equations

$$\begin{aligned} \kappa \nabla^4 w + \frac{1}{R_0} \frac{1}{r} \partial_r (r \psi) - \frac{1}{r} \partial_r (\psi \partial_r (w + w_I)) \\ = -p - \frac{F}{2\pi} \frac{\delta(r)}{r}, \end{aligned} \quad (87)$$

$$\frac{1}{Y} r \partial_r \left[\frac{1}{r} \partial_r (r \psi) \right] = \frac{r}{R_0} \partial_r w - \frac{1}{2} (\partial_r w)^2 - (\partial_r w) (\partial_r w_I), \quad (88)$$

which generalize Eqs. (3) and (4) in the presence of imperfections.

As in Eq. (5), we can absorb the effect of the pressure p in Eq. (87) into a uniform precompression $\psi(r) = \psi_0(r) = -pR_0r/2$ (corresponding to stresses $\sigma_{rr} = \sigma_{\phi\phi} = \sigma_0 = -pR_0/2$) and consider changes with respect to this prestress by substituting $\psi(r) \rightarrow \psi_0(r) + \psi(r)$ [see Eq. (B7) in Appendix B]. Also nondimensionalization (6) proceeds as before. Integrating on both sides from ρ to infinity finally gives

$$\begin{aligned} -\rho \partial_\rho (\nabla_\rho^2 \bar{w}) - \rho \bar{\psi} + \bar{\psi} \partial_\rho (\bar{w} + \bar{w}_I) - 2 \frac{p}{p_c} \rho \partial_\rho \bar{w} \\ = \frac{\bar{F}}{2\pi} + 2 \frac{p}{p_c} \rho \partial_\rho \bar{w}_I, \end{aligned} \quad (89)$$

which has to be solved together with the compatibility condition

$$\rho \partial_\rho \left[\frac{1}{\rho} \partial_\rho (\rho \bar{\psi}) \right] = \rho \partial_\rho \bar{w} - \frac{1}{2} (\partial_\rho \bar{w})^2 - (\partial_\rho \bar{w}) (\partial_\rho \bar{w}_I). \quad (90)$$

In comparison with our original Eqs. (10) for \bar{w} and the compatibility condition (8) for $\bar{\psi}$, there are three additional terms coupling to the imperfection displacement. The first term in Eq. (89) and the last term in Eq. (90) are couplings caused by the non-linearities of the shallow shell equations and are of order $O(\bar{z}\bar{z}_I)$ if \bar{z}_I is the amplitude of the imperfection displacement. They correct the homogeneous part of the shallow shell equations. The term $-2(p/p_c)\rho\bar{w}'_I = O(\bar{z}_I)$ in Eq. (89), on the other hand, is of lower order and corrects the inhomogeneity of the shallow shell equations. It can be interpreted as an additional effective pointlike force, which is localized to the extent of the imperfection \bar{w}_I and is caused by the response of the imperfection displacement to additional pressure. The effective force term gives the leading order effect of imperfections as long as $\bar{z} \lesssim 1$. This is a first hint that the combination of pressure and imperfection displacement leads to similar indentation behavior as a preindenting point force.

B. The avoided buckling bifurcation

In the following, we consider axially symmetric imperfections in the form of a localized indentation of Gaussian shape [15, 63]

$$\bar{w}_I(\rho) = -\delta e^{-\rho^2/\rho_I^2} \quad (91)$$

with dimensionless depth δ (measured in the same units as normal displacements w) and dimensionless size ρ_I (measured in the same units as radial distances r). In the presence of such imperfections, the critical pressure is reduced to $p_{c,\delta} < p_c$ because it is easier to buckle the preindented shell, in which an indentation imperfection displacement \bar{w}_I with $\bar{w}'_I > 0$ leads to additional compressive strains upon compression by pressure.

The numerical results in Fig. 14 show that the effect of the preindentation imperfection is indeed qualitatively very similar to the effect of a preindenting point force. For a localized imperfection field \bar{w}_I , the additional inhomogeneous term in Eq. (89), which is the leading order effect for $\bar{z} \lesssim 1$, becomes a localized effective force, which acts essentially in the same way as a preindenting point force. Therefore, we find the same bifurcation behavior as discussed in the previous section for a preindenting point force. The imperfection gives rise to an *avoided* or *perturbed bifurcation* at a reduced critical pressure $p_{c,\delta} < p_c$, and the bifurcation at $p_{c,\delta}$ becomes a saddle-node bifurcation, in which two stationary states emerge (see also Fig. 12): a stable preindented spherical state with energy \bar{E}_{sph} and indentation \bar{z}_{sph} and the unstable barrier state with energy \bar{E}_B and indentation $\bar{z}_B (> \bar{z}_{\text{sph}})$.

In the numerical approach, we solve the modified shallow shell equations as given explicitly in Eqs. (B8) and (B9) in Appendix B. In the presence of imperfections, the total energy difference in Eq. (12) is no longer the barrier energy but measures the energy difference between the barrier state or the preindented spherical state with $\bar{F} = 0$ and the unindented and precompressed state (with the same pressure but $\bar{F} = 0$ and $\bar{w} = 0$), which is no longer a stationary state satisfying the force balance (87) but which is still an admissible and well-defined shell state satisfying the compatibility condition (90). The total energy difference $\Delta \bar{E}_{\text{tot,imp}}$ to this state can be obtained analytically; see Eq. (B11) in Appendix B. In order to calculate the barrier energy $\bar{E}_{B,\delta} = \bar{E}_B - \bar{E}_{\text{sph}}$, we calculate this total energy difference for the barrier and the preindented spherical state numerically and use $\bar{E}_{B,\delta} = \Delta \bar{E}_{\text{tot,imp,B}} - \bar{E}_{\text{tot,imp,sph}}$ to directly access the energy barrier by continuation methods without the need to numerically integrate the force-indentation relation. Our numerical shallow shell theory results for the indentation as a function of the pressure agree well with results from moderate rotation theory [15, 63].

For small imperfection indentations $\delta \ll 1$, the bifurcation still occurs close to p_c and for small indentations \bar{z} . Then we employ the same expansion (54) as in Sec.

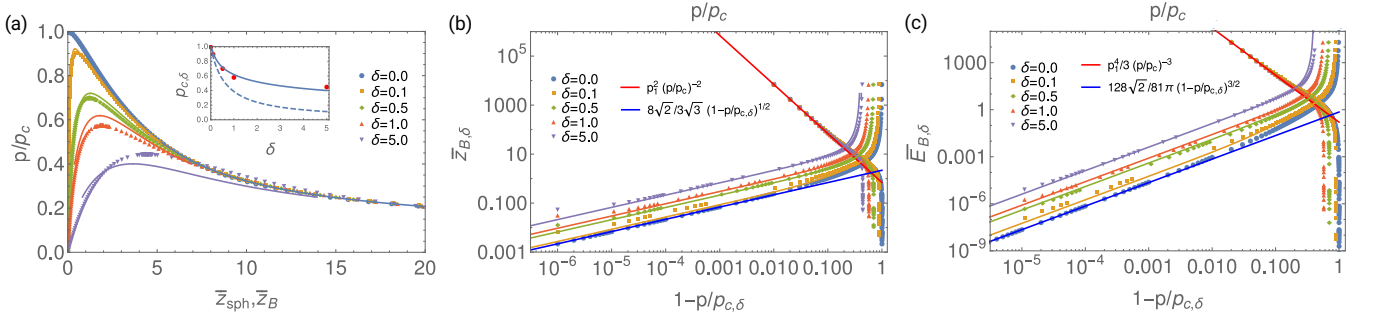


FIG. 14. (a) Bifurcation of the indentation as a function of the pressure for an imperfect shell with different imperfection depths δ (and size $\rho_I = 1$). Below a critical pressure $p_{c,\delta}$, two branches of shapes emerge in a saddle-node bifurcation, an indented spherical branch with \bar{z}_{sph} , and an unstable barrier state with \bar{z}_B . Lines: Approximation with effective preindenting force (94) and (95). Inset: Knockdown factor $p_{c,\delta}/p_c$ as a function of δ as compared to approximations with effective preindenting force (94) and (95) (solid line) and small δ approximation (93) together with (79) (dashed line). (b) Indentation difference $\bar{z}_{B,\delta} = \bar{z}_B - \bar{z}_{\text{sph}}$ as a function of pressure p/p_c (upper curves and upper horizontal scale) together with the analytical result (33a) for $\delta = 0$ (red line) and as a function of $1 - p/p_c$ (lower curves and lower horizontal scale) together with the analytical result (53a) for $\delta = 0$ (blue line). Lines are approximations with effective preindenting force (94) and (95). (c) Energy barrier $\bar{E}_{B,\delta}$ as a function of pressure p/p_c (upper curves and upper horizontal scale) together with the analytical result (33e) for $\delta = 0$ (red line) and as a function of $1 - p/p_{c,\delta}$ (lower curves and lower horizontal scale) together with the analytical result (53e) for $\delta = 0$ (blue line). Lines are approximations with effective preindenting force (94) and (95).

VI for shallow dimples and find in the leading order

$$\hat{M} \begin{pmatrix} \bar{w}'_{\text{lin},0} \\ \bar{\psi}_{\text{lin},0} \end{pmatrix} + \begin{pmatrix} 2(1-p/p_c)\bar{w}'_{\text{lin},0} + \bar{\psi}_{\text{lin},0}\bar{w}'_I \\ \bar{w}'_{\text{lin},0}\bar{w}'_I \end{pmatrix} = \begin{pmatrix} F_0 + \bar{z}^{-1}2(p/p_c)\rho\bar{w}'_I \\ 0 \end{pmatrix}.$$

Scalar multiplication with $(\bar{w}'_0, \bar{\psi}_0)$ on both sides gives the solvability condition

$$F_0 = \frac{2\sqrt{2}}{\pi}(1-p/p_c)^{1/2} + 2 \int d\rho\bar{w}'_I(\bar{\psi}_0\bar{w}'_0) - \bar{z}^{-1}2(p/p_c) \int d\rho\rho\bar{w}'_I\bar{w}'_0,$$

with an additional \bar{z}^{-1} contribution to the leading order, which means an additional imperfection force and an additional imperfection contribution to the linear stiffness. Both contributions are linear in the imperfection displacement \bar{w}_I . We evaluated integrals approximately in the limit $p \rightarrow p_c$ as previously done in Eq. (59). The force-displacement relation becomes

$$\bar{F} + (p/p_c)\bar{A}_I = \left(4\sqrt{2}(1-p/p_c)^{1/2} + \bar{k}_I\right)\bar{z} - \frac{3\sqrt{3}}{2}\bar{z}^2 + O(\bar{z}^3) \quad \text{with} \quad (92a)$$

$$\bar{A}_I \equiv 4\pi \int d\rho\rho\bar{w}'_I\bar{w}'_0, \quad (92b)$$

$$\bar{k}_I \equiv 4\pi \int d\rho\bar{w}'_I(\bar{\psi}_0\bar{w}'_0) = 4\pi \int d\rho\rho\bar{w}'_I\bar{w}'_0\bar{\sigma}_{rr,0}. \quad (92c)$$

Both imperfection modifications have a transparent physical interpretation. The strength of the imperfection

force $(p/p_c)\bar{A}_I$ is proportional to the pressure and the amplitude of the imperfection displacement but also depends on the “overlap area” of the imperfection field $\bar{w}_i(\rho)$ and the indentation mode \bar{w}_0 for $p = p_c$ and $\bar{F} = 0$ centered at the pole. Imperfections localized away from the pole will greatly reduce the imperfection force because \bar{w}'_I hardly overlaps with the indentation mode \bar{w}'_0 . The imperfection contribution \bar{k}_I to the linear stiffness is the overlap area weighted by the radial stress $\sigma_{rr,0}$ profile at $p = p_c$.

The buckling bifurcation is now governed by the presence of the additional z -independent imperfection force in the force-displacement relation, which acts analogously to a preindentation force $\bar{F}_{\text{pre}} = (p/p_c)\bar{A}_I$. For the imperfections with shape (91) we can explicitly evaluate \bar{A}_I in Eq. (92b) as

$$\bar{A}_I = 2\pi\delta\rho_I^2 \left(1 - \frac{\sqrt{\pi}}{2}\rho_I e^{-\rho_I^2/8} I_{1/2} \left(\frac{\rho_I^2}{8}\right)\right), \quad (93)$$

where $I_\nu(x)$ is the modified Bessel function. This reveals that, for fixed indentation depth δ , the overlap area \bar{A}_I and thus the imperfection force $\bar{F}_{\text{pre}} = (p/p_c)\bar{A}_I$ become maximal for an imperfection size $\rho_I \approx 2$, i.e., if the imperfection has twice the size of the elastic length $l_{\text{el}} = (hR_0)^{1/2}k^{-1}$ (see inset of Fig. 15). We conclude that this imperfection size is most effective in reducing the buckling threshold. This is confirmed by our numerical data in Fig. 15.

The description by an effective preindentation force $\bar{F}_{\text{pre}} = (p/p_c)\bar{A}_I$ also implies that the softening behavior of the shell close to the critical pressure $p_{c,\delta}$ is *universal* and the indentation difference $\bar{z}_{B,\delta} = \bar{z}_B - \bar{z}_{\text{sph}}$ from spherical to barrier state and the energy barrier $\bar{z}_{B,\delta} = \bar{E}_B - \bar{E}_{\text{sph}}$ are governed by the same exponents $\bar{z}_{B,\delta} \propto$

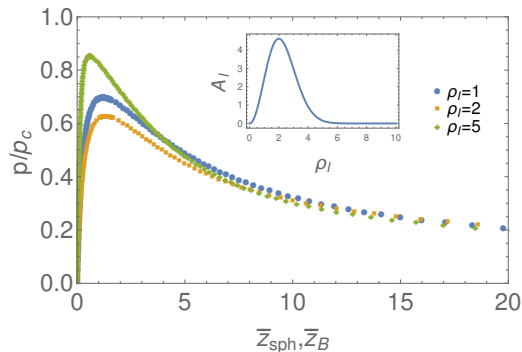


FIG. 15. Indentation as a function of the pressure for an imperfect shell with fixed imperfection depth $\delta = 0.5$ as a function of the imperfection size $\rho_I = 1$. The knockdown factor $p_{c,\delta}/p_c$ is maximal for $\rho_I \sim 2$. Inset: Overlap area A_I as a function of ρ_I for $\delta = 0.5$ according to Eq. (93) with a maximum at $\rho_I = 2$.

$\Delta\bar{p}^{1/2}$ and $\bar{E}_{B,\delta} \propto \Delta\bar{p}^{3/2}$ [$\Delta\bar{p} \equiv (p_{c,\delta} - p)/p_c$] as for a preindenting point force \bar{F}_{pre} or as in the absence of a preindenting point force.

We can use the results of the previous section with an effective preindenting force $\bar{F}_{\text{pre}} = (p/p_c)\bar{A}_I$ given by Eqs. (92b) or (93) to describe the avoided bifurcation in the presence of imperfections. This is quantitatively correct only for small δ [$\delta < 0.1$, see also inset in Fig. 14(a)] such that $p_{c,\delta}$ remains close to p_c . Our numerical results show, however, that the concept of an effective preindenting force $\bar{F}_{\text{pre}} = (p/p_c)\bar{A}_I$, which is given by an “overlap area” area \bar{A}_I can be generalized for larger δ and smaller p , if we replace the shallow shell solution in the linear approximation $\bar{w}_0 = \lim_{p \rightarrow p_c} \bar{w}_{\text{lin}}/\bar{z}$ [see Eqs. (56) and (54)] in Eq. (92b) by the general solution \bar{w}/\bar{z} . The resulting effective preindenting force

$$\bar{F}_{\text{pre}} = (p/p_c)\bar{A}_I = (p/p_c)4\pi \int d\rho \rho \bar{w}'_I \frac{\bar{w}'}{\bar{z}} \quad (94)$$

can describe our numerical data for the modified bifurcation behavior in Fig. 14 well for $0.05 \lesssim \delta \lesssim 1.0$ when we evaluate \bar{A}_I using the mirror-inverted Pogorelov dimple with $\bar{w}(\rho) = -\bar{z} + \rho^2$, which gives

$$\bar{A}_I = 8\pi\delta \frac{\rho_I^2}{\bar{z}} \left(1 - e^{-\bar{z}/\rho_I^2} \left(\frac{\bar{z}}{\rho_I^2} + 1 \right) \right), \quad (95)$$

and when we use $\bar{z} = \bar{z}_{B,0}$ as given by the interpolation formula (74).

Also analogously to a preindenting force, effects of imperfections are negligible for the deeply-indented barrier states in the Pogorelov limit $\bar{z}_B \gg 1$ and $p \ll p_c$, where elastic and pressure terms dominate the force-indentation relation (51). The indentation difference from spherical to barrier state $\bar{z}_{B,\delta} \approx \bar{z}_B$ and the barrier energy $\bar{E}_{B,\delta} \approx \bar{E}_B$ approach the Pogorelov asymptotics (33a) and (33e) in the Pogorelov limit for $p/p_c \ll 1/F_{\text{pre}}^{1/2}$ with

the effective \bar{F}_{pre} from Eq. (94), which is also seen in the numerical data in Fig. 14.

XIII. DISCUSSION AND CONCLUSION

We characterized the buckling bifurcation of closed spherical shells in the framework of continuum elastic theory under the combined action of pressure and point forces. Spherical shells have numerous realizations on the micro- and macroscale to which our theory applies.

Typical artificial micrometer-sized capsules have shell thicknesses of $h \sim 10\text{nm}$ and are made from soft materials with bulk Young moduli $E \sim 0.1\text{GPa}$. This results in 2D Young’s moduli $Y = Eh \sim 1\text{N/m}$ and bending moduli $\kappa \sim Eh^3 \sim 10^{-16}\text{Nm} \sim 2 \times 10^4 k_B T$ in agreement with elastometry measurements [53]. For $R_0 = 10\mu\text{m}$, typical Föppl-von Kármán numbers (2) are $\gamma \sim 10^6 - 10^7$.

Related but distinct systems are red blood cells, viruses, and biological cells. Red blood cells and viruses also have stretching, shear and bending elasticity featuring elastic moduli similar to artificial spherical microcapsules. Red blood cells are also micrometer-sized with a somewhat smaller shear modulus $\mu \sim 10^{-5}\text{N/m}$ and bending moduli $\kappa \sim 10^{-16}\text{Nm}$ [27, 28]. One important difference from artificial microcapsules is the local inextensibility of the lipid bilayer membrane of the red blood cell, which enforces a local area constraint such that lipid membranes and red blood cells are even less extensible than shells [27]. Furthermore, there are differences in the rest shape. The buckling of spherical shells is governed by their spherical rest shape, which has minimal area at given volume. Thus, any deformation stretches the shell, which leaves the mirror-inverted Pogorelov dimple as preferred buckled shape under pressure. Red blood cells have a fixed volume V_0 and fixed area A_0 combining to a reduced volume $v_{\text{RBC}} = V_0/(4\pi/3)(A_0/4\pi)^{3/2} \sim 0.6$ and an oblate spheroidal rest shape under physiological conditions, while the reduced volume of a sphere reaches the maximal value $v_{\text{sph}} = 1$. Under point-force indentation, the reduced volume of a spherical shell only reduces to $v = 1 - O(\gamma^{-1})$ up to the barrier. The additional area that is available in a nonspheroidal rest shape with $v_{\text{RBC}} < 1$ contributes to the rich deformation behavior of red blood cells [27–30]. Another crucial difference is the role of spontaneous curvature (or the conjugate integrated mean curvature or area difference) as control parameter. For red blood cells, area difference is an important control parameters of shape sequences [28–30] whereas spherical shells are treated with a fixed spontaneous curvature given by the spherical rest shape (only recently, Pezulla *et al.* started to address the role of spontaneous curvature in buckling of spherical shells [64]). Viruses range in size from 15 to 500nm and have elastic moduli $Y = Eh \sim 0.1 - 1\text{N/m}$ and bending moduli $\kappa \sim Eh^3 \sim 5 \times 10^{-19}$ to $5 \times 10^{-15}\text{Nm}$ [65], similar to artificial microcapsules. Viruses are, however, crystalline spherical shells consisting of discrete pro-

tein building blocks. On a sphere, the crystal structure must contain topologically unavoidable triangulation defects. This results in faceted equilibrium shapes of large viruses with Föppl-von Kármán numbers $\gamma > 150$, while only small viruses maintain a spherical equilibrium shape [31]. Therefore, our results regarding, for example, the linear stiffness k apply only to small viruses [65].

For pressurized spherical shells, we showed that nonlinear shallow shell theory can quantify many aspects of the energy barrier, which has to be overcome if buckling is triggered by “poking” with a point force F while the pressure is still subcritical, i.e., below the classical buckling pressure p_c . In particular, we could derive the exact asymptotics of the energy barrier properties (including the numerical prefactors) in two relevant limiting regimes, namely in the Pogorelov limit at small pressures $p \ll p_c$, where the indentation at the transition state is much deeper than shell thickness, $z_B \gg h$, and in the opposite limit for pressures very close to p_c , where the indentation at the transition state is shallow, $z_B \ll h$, and develops oscillations. We developed a very accurate numerical approach, which is based on the closed analytical expression (12) for the energy barrier height and allows us to trace the energy barrier height by numerical continuation techniques. The numerical study reveals that there are only these two regimes for all barrier properties, such as the barrier energy E_B , the indentation depth z_B , the indentation volume $\Delta\bar{V}_B$, and the indentation width ρ_B , with a clear crossover if the indentation $z_B \sim h$ or $\bar{z}_B \sim 1$ in dimensionless units (6).

Using systematic expansions of the nonlinear shallow shell equations about the Pogorelov mirror-inverted dimple for $p/p_c \ll 1$ and the linear response state for $(1 - p/p_c) \ll 1$, we obtained a complete analytical characterization of the energy barrier in both limits; see Eqs. (33) for the Pogorelov limit and Eqs. (53) for pressures close to p_c . The analytical results agree with our numerical shallow shell data over several decades of control parameters p/p_c or $1 - p/p_c$, respectively (see Figs. 5 and 7) and allow us to formulate quantitatively correct interpolation formulas for the barrier energy \bar{E}_B and the corresponding indentation \bar{z}_B [Eqs. (73) and (74), respectively], which incorporate all analytical constraints.

Reverting the nondimensionalization (6) gives $E_B = YR_0^2\gamma^{-3/2}2\pi f_p(p/p_c)$, and we can estimate values for the energy barrier in applications. The typical barrier energy scale is $E_B \propto YR_0^2\gamma^{-3/2} = (\kappa^3/YR_0^2)^{1/2} = [12(1 - \nu^2)]^{-3/2}EhR_0^2(h/R_0)^3$ with a pressure-dependent numerical prefactor $2\pi f_p(p/p_c)$, which is given by the interpolating function (73). For $p = p_c/2$ at half the buckling pressure, $2\pi f_p(1/2) \simeq 18$. For a typical artificial thin microscale capsule with $R_0 = 10\mu\text{m}$, $h = 10\text{nm}$ made from a soft material with $E = 0.1\text{GPa}$ with $\nu = 1/2$ this gives an energy barrier $E_B \sim 17k_B T$ at room temperature or $E_B/U_c = 2.4 \times 10^{-4}$, where $U_c = \frac{1}{2}p_c\Delta V_c = 16\pi(1 - \nu)\kappa$ is the elastic energy stored in the spherical shape just before it buckles. These estimates demonstrate that the buckling energy barrier is

rather small: It is comparable to the thermal energy and much smaller than the total elastic energy stored in the capsule. Therefore, capsules become very susceptible to thermally induced buckling [9, 12], small point forces, or imperfection effects already at moderate compressive pressures. The typical normal indentation at the barrier is $z_B \propto R_0\gamma^{-1/2} = h/[12(1 - \nu^2)]^{1/2}$, i.e., the shell thickness. The pressure-dependent numerical prefactor $g_p(p)$ is given by the interpolation function (74) with $g_p(1/2) \simeq 1.7$ at $p = p_c/2$. This demonstrates that only small indentations have to be achieved to overcome the energy barrier.

We also obtain a complete picture of the buckling energy landscapes (34) and (52) in both regimes, i.e., the total indentation energy \bar{E}_{ind} as a function of the indentation \bar{z} , from which also the force-displacement curves can be calculated in both regimes. In the Pogorelov limit we could show the equivalence of our systematic expansion of the nonlinear shallow shell equations about the Pogorelov mirror-inverted dimple to a boundary layer approach by Evkin *et al.* [21] and establish the connection to and generalize recent work of Gomez *et al.* [19] on the $p = 0$ case. While Gomez *et al.* addressed the case $F > 0$ and $p = 0$, our analytical calculation focused on the barrier state, where $F = 0$, for arbitrary $0 \leq p \leq p_c$. We could draw conclusions for the general case by showing that both results are consistent if the elastic part of the indentation energy is *independent of the pressure*. Future work should try to develop a systematic expansion covering the full behavior for $F > 0$ and $0 \leq p \leq p_c$.

The regime $\bar{z}_B \ll 1$ for p close to p_c is particularly interesting as it characterizes the “critical properties” if the buckling instability is approached from below. In this regime close to p_c , we find a softening of the spherical shell, which is characterized by three critical exponents: (i) the stiffness k for the linear response to point forces vanishes $\propto (1 - p/p_c)^{1/2}$; (ii) the buckling energy barrier maximum vanishes $\propto (1 - p/p_c)^{3/2}$; and (iii) the shell indentation at the energy barrier maximum vanishes $\propto (1 - p/p_c)^{1/2}$. These results are shown analytically and agree with our numerical shallow shell data. They extend and correct previous findings in Ref. [9], which were based on less accurate SURFACE EVOLVER simulations.

The linear stiffness k with respect to a point force is experimentally accessible in mechanical compression tests such as plate compression [49, 50] or compression by microscopy tips [50, 51] because all of these compression devices effectively act as point forces in the initial regime. Therefore our result (21) for the softening of the shell can be directly tested if such compression tests are combined with external pressure p . For microcapsules in liquids external pressure can be generated as osmotic pressure [17], and for macroscopic capsules as mechanical air or liquid pressure. For compressive pressure $p = p_c/2$ at half the buckling pressure, Eq. (21) predicts that the stiffness reduces to only 64% of its pressure-free value $k = 8Y\gamma^{-1/2}$. Measurements of the linearized stiffness at two different pressures can also be used to infer two unknown quanti-

ties, for example, the shell's Young's modulus and capsule pressure via Eq. (21) and, thus, determine elastic properties of the shell. While the linear stiffness increases for pressurized shells [52], it decreases for shells under compressive pressures. In Ref. [55], it has been shown that a positive interfacial tension also acts as a stretching pressure and gives rise to linear stiffening. Softening can therefore also be induced by a negative interfacial tension. This shows that active expansion or stretching tensions generated in biological cells by molecular motors in the cell cortex, which will give rise to negative interfacial tension in the cortex, will effectively soften the cell.

Knowledge of the buckling energy landscape also enables us to calculate the Maxwell pressure $p_{c1} \sim p_c \gamma^{-1/4}$ and the critical unbuckling pressure $p_{cu} \sim 3p_{c1}/4$ from shallow shell theory. The buckling energy landscape also suggests that soft spots, which are small compared to the elastic length $l_{el} = (R_0 h)^{1/2}$ will immediately unbuckle for p smaller than p_c and thus exhibit no hysteresis in buckling and unbuckling.

Our results shed light on the nature of the buckling bifurcation as schematically shown in Fig. 12. The bifurcation at $p = p_c$ is a subcritical bifurcation which has a fixed point structure similar to a subcritical pitchfork bifurcation. The barrier states are a subcritical branch of unstable stationary points, which appear together with the buckled snap-through state for $p > p_{cu}$ in a type of saddle-node or fold bifurcation. The snap-through state becomes the only minimum after the bifurcation at $p = p_c$. Within the pressure window $p_{cu} < p < p_c$ there is bistability between buckled and unbuckled solutions with the barrier state separating these two stable branches resulting in hysteresis. Upon approaching the instability from $p < p_c$, the softening of the shell with vanishing linear stiffness and energy barrier can give rise to important dynamical consequences such as a ‘‘critical slowing down’’ of the buckling dynamics [62]. A complete theory of the buckling dynamics of a shell close to p_c remains to be developed.

This bifurcation behavior is modified if a preindenting point force F_{pre} is applied or in the presence of localized axisymmetric imperfections of indentation depth δ and size r_I . Both the numerical shallow shell analysis and the analytical approach could be extended to these situations. Interestingly, a localized preindentation imperfection's effect on the buckling instability is very similar to that of a preindenting point force, as can be immediately recognized by comparing Figs. 13 and 14. For both cases, the buckling bifurcation becomes an avoided or perturbed bifurcation at a reduced critical pressure $p_{c,F} < p_c$ or $p_{c,\delta} < p_c$. Below this critical pressure, two stationary states emerge in a saddle-node bifurcation, namely a stable quasi-spherical state and an unstable barrier state. Interestingly, the softening behavior sketched above with (ii) the buckling energy barrier between quasiperfect and barrier state vanishing as $\bar{E}_B \propto \Delta\bar{p}^{3/2}$ and (iii) the shell indentation difference between quasiperfect and barrier state vanishing

$\delta\bar{z}_B \propto \Delta\bar{p}^{1/2}$ remains universally valid both in the presence of a preindenting force and imperfections. This also suggests that (i) remains valid, and the linear stiffness vanishes as $k \propto \bar{E}_B/\delta\bar{z}_B^2 \propto \Delta\bar{p}^{1/2}$.

We were able to make the equivalence between preindenting point force and imperfections quantitative with Eq. (94) and found that imperfections effectively act as a point force proportional to the pressure p and an ‘‘overlap area’’ A_I , which depends on the shape of the imperfection $w_I(r)$ and the indentation $w(r)$. This allowed us to conclude that there exists an ‘‘optimal’’ size for an imperfection of $r_I = 2l_{el}$, where it maximizes the knockdown factor for the buckling pressure. The quantitative prediction (94) may be useful in designing spherical shells with specific buckling thresholds.

Appendix A: Derivation of total energy difference

The difference in total energy $\Delta E_{tot} = \Delta E_s + \Delta E_b + p\Delta V$ (i.e., the sum of stretching and bending energy and mechanical work by pressure) between the indented barrier state ($F = 0$) and the precompressed unindented spherical state (with the same pressure but $\bar{z} = 0$) is given by the simple, explicit formula (12):

$$\Delta\bar{E}_{tot} = \bar{E}_B = -\frac{1}{4} \int_0^\infty d\rho \bar{\psi}(\bar{w}')^2, \quad (\text{A1})$$

where $\bar{\psi}$ and \bar{w} are solutions of the shallow shell equations (7) and (8) in the barrier state with $\bar{F} = 0$.

More generally, for an arbitrary indented state with a point force F and a corresponding indentation z , the total energy difference $\Delta E_{tot,F} = \Delta E_s + \Delta E_b + p\Delta V - Fz$ between the indented state and the precompressed unindented spherical state (with the same pressure and $z = 0$) is given by

$$\Delta\bar{E}_{tot,F} = -\frac{1}{4} \int_0^\infty d\rho \bar{\psi}(\bar{w}')^2 - \frac{\bar{F}}{4\pi} \bar{z} - 2(1 + \nu) \frac{p}{p_c} \frac{\bar{F}}{2\pi}, \quad (\text{A2})$$

where $\bar{\psi}$ and \bar{w} are solutions of the shallow shell equations (7) and (8) for indentation $\bar{z} = -\bar{w}(0)$ and corresponding point force \bar{F} .

In order to derive these formulas, we start with the dimensionless elastic energy, i.e., stretching and bending energy of an axisymmetric state with stress function ψ and normal displacement \bar{w} in shallow shell theory [see also Eq. (B1) below] [16, 46],

$$\begin{aligned} E_{el} &= E_s + E_b \\ &= \frac{1}{2} \int d\rho \rho \left[\left(\bar{\psi}' + \frac{\bar{\psi}}{\rho} \right)^2 - 2(1 + \nu) \bar{\psi}' \frac{\bar{\psi}}{\rho} \right] \\ &\quad + \frac{1}{2} \int d\rho \rho \left[\left(\bar{w}'' + \frac{\bar{w}'}{\rho} \right)^2 - 2(1 - \nu) \bar{w}' \frac{\bar{w}}{\rho} \right]. \quad (\text{A3}) \end{aligned}$$

The stretching energy difference ΔE_s is the difference between the stretching energy due to the total stress function $\psi + \psi_0$ and the stretching energy due to the prestress $\psi_0 = -pR_0r/2$ [or $\bar{\psi}_0(\rho) = -2\rho p/p_c$],

$$\begin{aligned} \Delta \bar{E}_s &= \frac{1}{2} \int d\rho \rho \left[\left((\bar{\psi}_0 + \psi)' + \frac{\bar{\psi}_0 + \psi}{\rho} \right)^2 \right. \\ &\quad \left. - 2(1 + \nu)(\bar{\psi}_0 + \psi)' \frac{\bar{\psi}_0 + \psi}{\rho} \right. \\ &\quad \left. - \left(\bar{\psi}_0' + \frac{\bar{\psi}_0}{\rho} \right)^2 + 2(1 + \nu)\bar{\psi}_0' \frac{\bar{\psi}_0}{\rho} \right] \\ &= \frac{1}{2} \int d\rho \rho \left[\left(\bar{\psi}' + \frac{\bar{\psi}}{\rho} \right)^2 \right] + 2(1 - \nu) \frac{\bar{F}}{2\pi} \frac{p}{p_c}, \quad (\text{A4}) \end{aligned}$$

where we used $\bar{\psi} = 0$ for $\rho = 0$ and $\rho = \infty$ and the asymptotics (9). The last term vanishes at the barrier state, where $\bar{F} = 0$. For the bending energy difference, we find (note that w was already defined as the normal displacement relative to the precompressed state)

$$\Delta \bar{E}_b = \frac{1}{2} \int d\rho \rho \left[\left(\bar{w}'' + \frac{\bar{w}'}{\rho} \right)^2 \right], \quad (\text{A5})$$

where we used $\bar{w}' = 0$ for $\rho = 0$ and $\rho = \infty$. The dimensionless mechanical work is

$$\overline{p\Delta V} = 4 \frac{p}{p_c} \int d\rho \rho \bar{w} = \frac{2}{\pi} \frac{p}{p_c} \overline{\Delta V} \quad (\text{A6})$$

(again, note that w was defined as the normal displacement relative to the precompressed state).

Using partial integration [with $\bar{w}(\infty) = 0$ and $\bar{w}'(0) = 0$], the relation (10), and $\int d\rho \bar{w}' = -\bar{w}(0) = \bar{z}$, we can re-write $\Delta \bar{E}_b$ as

$$\Delta \bar{E}_b = \frac{1}{2} \int d\rho \left[\rho \bar{\psi} \bar{w}' - \bar{\psi} (\bar{w}')^2 + 2 \frac{p}{p_c} \rho \bar{w}' \right] + \frac{\bar{F}}{2\pi} \frac{1}{2} \bar{z}.$$

With Eq. (11), we obtain

$$\begin{aligned} \Delta \bar{E}_b &= -\overline{p\Delta V} + \frac{1}{2} \int d\rho \rho \bar{\psi} \bar{w}' \left(1 - \frac{\bar{w}'}{\rho} \right) \\ &\quad + \frac{\bar{F}}{2\pi} \left(-4 \frac{p}{p_c} + \frac{1}{2} \bar{z} \right). \end{aligned}$$

This results in a total energy difference

$$\begin{aligned} \Delta \bar{E}_{\text{tot,F}} &= \Delta \bar{E}_s + \Delta \bar{E}_b + \overline{p\Delta V} - \frac{\bar{F}}{2\pi} \bar{z} \\ &= \frac{1}{2} \int d\rho \rho \left[\left(\bar{\psi}' + \frac{\bar{\psi}}{\rho} \right)^2 + \bar{\psi} \bar{w}' \left(1 - \frac{\bar{w}'}{\rho} \right) \right] \\ &\quad + \frac{\bar{F}}{2\pi} \left(2(1 - \nu) \frac{p}{p_c} - 4 \frac{p}{p_c} + \frac{1}{2} \bar{z} - \bar{z} \right) \\ &= -\frac{1}{4} \int_0^\infty d\rho \bar{\psi} (\bar{w}')^2 - \frac{\bar{F}}{4\pi} \bar{z} - 2(1 + \nu) \frac{p}{p_c} \frac{\bar{F}}{2\pi}, \end{aligned}$$

where we used the compatibility condition (8). This is Eq. (A2) and specializes to Eq. (A1) at the barrier where $\bar{F} = 0$.

A further generalization to shells containing imperfections is given in Appendix B.

Appendix B: Nonlinear shallow shell equations with imperfections

1. Derivation of shallow shell equations

We follow Refs. [10, 13, 15, 63] and consider imperfections in form of a normal axisymmetric displacement field w_I , which is already present in the strain-free state of the shell. With a displacement field $\mathbf{u} = u\mathbf{e}_x + v\mathbf{e}_y + w\mathbf{e}_z$, where x and y are Cartesian directions in the two-dimensional reference plane over which shallow shell configurations are parametrized and \mathbf{e}_z is the outward pointing normal, the in-plane strain tensor in the presence of the imperfection field is given by $u_{ij} = u_{ij}(w + w_I) - u_{ij}(w_I)$, resulting in

$$u_{xx} = \partial_x u + \frac{1}{2} (\partial_x w)^2 + \frac{w}{R_0} + \partial_x w \partial_x w_I$$

$$u_{yy} = \partial_y v + \frac{1}{2} (\partial_y w)^2 + \frac{w}{R_0} + \partial_y w \partial_y w_I$$

$$u_{xy} = \frac{1}{2} (\partial_y u + \partial_x v + \partial_x w \partial_y w + \partial_x w \partial_y w_I + \partial_x w_I \partial_y w).$$

These modified strains are used in the linear Hookean stress-strain relation

$$\sigma_{xx} = \frac{Y}{1 - \nu^2} (u_{xx} + \nu u_{yy}),$$

$$\sigma_{yy} = \frac{Y}{1 - \nu^2} (u_{yy} + \nu u_{xx}),$$

$$\sigma_{xy} = \frac{Y}{1 - \nu} u_{xy},$$

which is unaffected by imperfections. The changes in the curvature tensor $k_{ij} = k_{ij}(w + w_I) - k_{ij}(w_I)$ due to normal displacement are independent of w_I ,

$$k_{ij} = \partial_i \partial_j w,$$

in linear order. Imperfections thus only affect the in-plane strain tensor u_{ij} via the nonlinear term in the normal displacement w .

Also, in the presence of imperfections the Hookean elastic energy is given by the sum of stretching and bending energies:

$$E_{el} = \int dx dy (e_s + e_b) \quad (\text{B1})$$

$$\begin{aligned} e_s &= \frac{Y}{2(1 - \nu^2)} [(u_{xx} + u_{yy})^2 - 2(1 - \nu)(u_{xx}u_{yy} - u_{xy}^2)], \\ e_b &= \frac{\kappa}{2} [(\partial_x^2 w + \partial_y^2 w) - 2(1 - \nu)(\partial_x^2 w \partial_y^2 w - (\partial_x \partial_y w)^2)]. \end{aligned}$$

TABLE I. Units for nondimensionalization and dimensionless quantities.

	Here	Gomez <i>et al.</i> [19]	Hutchinson <i>et al.</i> [4, 7]	Evkin <i>et al.</i> [5, 21]
Norm. displacement unit	$(\kappa/Y)^{1/2} = R_0\gamma^{-1/2}$ $= hk^{-2}$	h	$\Delta w_R \equiv \sqrt{12}hk^{-2}$ $= h(1-\nu^2)^{-1/2}$	
Norm. displacement	$\bar{w} \equiv wk^2/h$	$W = \bar{w}k^{-2}$	$\Delta w/\Delta w_R = \xi g(\bar{s}, \xi)$ $= -\bar{w}/\sqrt{12}$	
Indentation depth	$\bar{z} \equiv -\bar{w} _{\rho=0}$	$\Delta \equiv -W _{\rho=0} = \bar{z}k^{-2}$	$\xi \equiv \Delta w/\Delta w_R _{\bar{s}=0} = \bar{z}/\sqrt{12}$	$\varepsilon^{-2} = \bar{z}/4$
Pressure	p/p_c	$p = 0$	$p/p_c = f(\xi)$	$\bar{q} = p/p_c$
Radial distance unit	$(\kappa R_0^2/Y)^{1/4} = R_0\gamma^{-1/4}$ $= (hR_0)^{1/2}k^{-1}$	$(hR_0)^{1/2}$	$12^{1/4}(hR_0)^{1/2}$	
Radial distance	$\rho \equiv rk/(hR_0)^{1/2}$	$\rho_{\text{Gomez}} = \rho k^{-1}$	$\bar{s} \simeq \rho/12^{1/4}$	
Indentation volume	$\Delta \bar{V}_B \equiv -2\pi \int_0^\infty d\rho \rho \bar{w}$	–	$\Delta \bar{V}_B = 24\pi h(\xi)$	
Force unit	$Y R_0/\gamma = \kappa/R_0$ $= (Yh^2/R_0)k^{-4}$	Yh^2/R_0	$2\pi\kappa/R_0$ [4]	
Force	\bar{F}	$F = \bar{F}k^{-4}$	$\bar{F}_{\text{Marthelot}} = \bar{F}/2\pi$ [4]	$\bar{Q} = \bar{F}/12\pi$
Energy unit	$e \equiv 2\pi(\kappa^3/YR_0^2)^{1/2}$	–	$W_c = \frac{1}{2}p_c\Delta V_c Ch/R_0 = 48e$ $= 96\pi(\kappa^3/YR_0^2)^{1/2}$ $C \equiv \frac{\sqrt{3}}{(1-\nu)\sqrt{1-\nu^2}}$	$U_A = \frac{1}{2}(p/p_c)^2 p_c \Delta V_c$
Barrier energy	\bar{E}_B	–	$W/W_c = \bar{E}_B/48$ $= q(\xi) - f(\xi)h(\xi)$	$\bar{E} = \frac{\bar{E}_B}{2(p/p_c)^2 \lambda^2 (1-\nu)}$ $\lambda^2 \equiv 4k^2 R_0/h$

Variation with respect to u and v gives

$$\partial_x \sigma_{xx} + \partial_y \sigma_{xy} = 0, \quad \partial_y \sigma_{yy} + \partial_x \sigma_{xy} = 0,$$

which is automatically satisfied by the introduction of the Airy stress function

$$\sigma_{xx} = -\partial_y^2 \Phi, \quad \sigma_{yy} = -\partial_x^2 \Phi, \quad \sigma_{xy} = \partial_x \partial_y \Phi. \quad (\text{B2})$$

These relations are unchanged in the presence of the imperfection field w_I .

The first nonlinear shallow shell equation [cf. Eq. (3)] for Φ and w is obtained from extremizing E_{el} with respect to w (and expressing stresses by the Airy stress function Φ) to get the elastic force in normal direction,

$$\kappa \nabla^4 w - \frac{1}{R_0} \nabla^2 \Phi + [\Phi, w + w_I] = -p - \frac{F}{2\pi} \frac{\delta(r)}{r}, \quad (\text{B3})$$

$$\text{where } [f, g] \equiv \partial_x^2 f \partial_y^2 g + \partial_y^2 f \partial_x^2 g - 2(\partial_x \partial_y f)(\partial_x \partial_y g).$$

By eliminating the displacement fields u and v from the stress-strain relation we obtain the additional compatibility condition [cf. Eq. (4)]. In the presence of imperfections we obtain

$$\begin{aligned} -\frac{1}{Y} \nabla^4 \Phi &= \partial_y^2 u_{xx} + \partial_x^2 u_{yy} - 2\partial_x \partial_y u_{xy} \\ &= \frac{1}{R_0} \nabla^2 w - \frac{1}{2} [w, w] - [w, w_I]. \end{aligned} \quad (\text{B4})$$

Both Eqs. (B3) and (B4) can be brought into a simpler form for axisymmetric shapes if coordinates r, ϕ are used.

For axisymmetric functions w, w_I, Φ that only depend on r , we can use $\nabla^2 \dots = (\frac{1}{r} \partial_r + \partial_r^2) \dots = \frac{1}{r} \partial_r r \partial_r \dots$ and

$$[f, g] = \frac{1}{r} \partial_r (\partial_r f \partial_r g).$$

If we also use the derivative of the stress function $\psi = -\partial_r \Phi$ (with $\sigma_{\phi\phi} = \psi'$ and $\sigma_{rr} = \psi/r$) and integrate eq. (B4) once, we find

$$\begin{aligned} \kappa \nabla^4 w + \frac{1}{R_0} \frac{1}{r} \partial_r (r\psi) - \frac{1}{r} \partial_r (\psi \partial_r (w + w_I)) \\ = -p - \frac{F}{2\pi} \frac{\delta(r)}{r}, \end{aligned} \quad (\text{B5})$$

$$\frac{1}{Y} r \partial_r \left[\frac{1}{r} \partial_r (r\psi) \right] = \frac{r}{R_0} \partial_r w - \frac{1}{2} (\partial_r w)^2 - (\partial_r w)(\partial_r w_I). \quad (\text{B6})$$

These are Eqs. (87) and (88) in the main text, which generalize the nonlinear shell equations (3) and (4) in the presence of imperfections. As in Eq. (5), we can absorb the effect of the pressure p in Eq. (B5) into a uniform precompression with $w(r) = w_0 < 0$ and $\psi(r) = \psi_0(r) = -pR_0 r/2$ (corresponding to stresses $\sigma_{rr} = \sigma_{\phi\phi} = \sigma_0 = -pR_0/2$) and consider changes with respect to this prestress by substituting $w(r) \rightarrow w_0 + w(r)$ and $\psi(r) \rightarrow \psi_0(r) + \psi(r)$. This gives

$$\begin{aligned} \kappa \nabla^4 w + \frac{1}{R_0} \frac{1}{r} \partial_r (r\psi) - \sigma_0 \nabla^2 (w + w_I) \\ - \frac{1}{r} \partial_r (\psi \partial_r (w + w_I)) = -\frac{F}{2\pi} \frac{\delta(r)}{r} \end{aligned} \quad (\text{B7})$$

in the presence of imperfections. We note that, in the presence of imperfections, a precompressed state with $w(r) = w_0 < 0$ and $\psi(r) = \psi_0(r) = -pR_0r/2$ is no longer a stationary state as it does *not* satisfy the force balance (B5). It is, however, an admissible shell state which satisfies the compatibility conditions (B6). Therefore, we can still consider all quantities relative to this state as for an ideal shell.

Non-dimensionalization proceeds as before using (6) and we obtain

$$\begin{aligned} \nabla_\rho^4 \bar{w} + \frac{1}{\rho} \partial_\rho (\rho \bar{\psi}) + 2 \frac{p}{p_c} \nabla_\rho^2 (\bar{w} + \bar{w}_I) \\ - \frac{1}{\rho} \partial_\rho (\bar{\psi} \partial_\rho (\bar{w} + \bar{w}_I)) = -\frac{\bar{F}}{2\pi} \frac{\delta(\rho)}{\rho} \quad (\text{B8}) \\ \rho \partial_\rho \left[\frac{1}{\rho} \partial_\rho (\rho \bar{\psi}) \right] = \rho \partial_\rho \bar{w} - \frac{1}{2} (\partial_\rho \bar{w})^2 - (\partial_\rho \bar{w}) (\partial_\rho \bar{w}_I), \quad (\text{B9}) \end{aligned}$$

with $\nabla_\rho^2 \dots = \frac{1}{\rho} \partial_\rho (\rho \partial_\rho \dots)$. In this form, the shallow shell equations are solved numerically in the presence of imperfections analogously to the ideal case.

We can also generalize the exact relations (10) and (11) for the imperfect shell and find the relation (89) in the main text and

$$-\frac{\bar{F}}{2\pi} = \int_0^\infty d\rho \rho \bar{w} + \int_0^\infty d\rho \rho \left[\frac{1}{4} (\bar{w}')^2 + \frac{1}{2} \bar{w}' \bar{w}'_I \right]. \quad (\text{B10})$$

2. Derivation of total energy difference

In the form (B8) and (B9), the shallow shell equations are solved numerically analogously to the ideal case. One numerical complication is the correct calculation of barrier energies without the need to numerically integrate force-indentation relations by a suitable generalization of the exact result (A1) for the total energy difference between the barrier state ($\bar{F} = 0$) and the precompressed unindented state (with $\bar{F} = 0$ and $\bar{w} = 0$, but which is no longer a stationary state in the presence of imperfections as discussed above) to the imperfect situation:

$$\Delta \bar{E}_{\text{tot,imp}} = -\frac{1}{4} \int_0^\infty d\rho \bar{\psi} (\bar{w}')^2 - \frac{p}{p_c} \int d\rho \rho \bar{w}' \bar{w}'_I. \quad (\text{B11})$$

We note that the last term can be written as $-[(p/p_c)\bar{A}_I/4\pi]\bar{z}$ with $\bar{A}_I \equiv 4\pi \int d\rho \rho \bar{w}'_I (\bar{w}'/\bar{z})$, which is analogously defined to the imperfection area occurring in the force-indentation relation (92a). Then the imperfection force $(p/p_c)\bar{A}_I$ in Eq. (B11) is analogous to the point force \bar{F} in the second term in Eq. (A2), which also corroborates the use of an effective preindenting force (94) in the presence of imperfections.

The derivation follows the same lines as in Appendix A without the imperfection field. We consider the total energy difference $\Delta E_{\text{tot}} = \Delta E_s + \Delta E_b + p\Delta V$ and expressions (A4) for the stretching energy $\Delta \bar{E}_s$, (A5) for the bending energy $\Delta \bar{E}_b$, and (A6) for the mechanical work $p\Delta V$ remain valid also in the presence of imperfections (we consider the case $\bar{F} = 0$ here).

Using partial integration and Eqs. (89) and (B10) we can rewrite $\Delta \bar{E}_b$ for $\bar{F} = 0$ as

$$\begin{aligned} \Delta \bar{E}_b = -\overline{p\Delta V} + \frac{1}{2} \int d\rho \rho \bar{\psi} \bar{w}' \left(1 - \frac{\bar{w}'}{\rho} \right) \\ - \frac{p}{p_c} \int d\rho \rho \bar{w}' \bar{w}'_I - \frac{1}{2} \int d\rho \bar{\psi} \bar{w}' \bar{w}'_I. \end{aligned}$$

Using (B9), this leads to the total energy difference (B11).

Appendix C: Dimensionless quantities

We provide a conversion table (Table I) for the different dimensionless quantities used here [see Eq. (6)], by Gomez *et al.* in Ref. [19], and by Hutchinson *et al.* in Refs. [4, 7, 10].

The shell thickness is called h . We define $k \equiv [12(1-\nu^2)]^{1/4}$ and the Föppl-von Kármán number $\gamma \equiv YR_0^2/\kappa = (R_0/h)^2 k^4$ [see Eq. (2)], and use the critical buckling pressure $p_c = 4(Y\kappa)^{1/2}/R_0^2 = 4(Yh/R_0^2)k^{-2}$ [see Eq. (1)]. Note that in the shallow shell approximation the arc length s used in Refs. [7, 10] approaches the radial coordinate r . In Refs. [7, 10], $C \equiv \sqrt{3}/(1-\nu)\sqrt{1-\nu^2}$ is used.

-
- [1] R. Zoelly, *Über ein Knickungsproblem an der Kugelschale* (Ph.D. thesis, ETH Zürich, Zürich, Switzerland, 1915).
 [2] D. Bushnell, *AIAA J.* **19**, 1183 (1981).
 [3] S. Knoche and J. Kierfeld, *Phys. Rev. E* **84**, 046608 (2011).
 [4] J. Marthelot, F. López Jiménez, A. Lee, J. W. Hutchinson, and P. M. Reis, *J. Appl. Mech.* **84**, 121005 (2017).
 [5] A. Y. Evkin and O. V. Lykhachova, *Int. J. Solids Struct.*

- 118-119**, 14 (2017).
 [6] J. W. Hutchinson and J. M. T. Thompson, *J. Appl. Mech.* **84**, 061001 (2017).
 [7] J. W. Hutchinson and J. M. T. Thompson, *Phil. Trans. R. Soc. A* **375**, 20160154 (2017).
 [8] J. M. T. Thompson, J. W. Hutchinson, and J. Sieber, *Int. J. Bifurc. Chaos* **27**, 1730048 (2017).
 [9] L. Baumgarten and J. Kierfeld, *Phys. Rev. E* **97**, 052801

- (2018).
- [10] J. W. Hutchinson and J. M. T. Thompson, *Int. J. Solids Struct.* **148-149**, 157 (2018).
- [11] E. Virost, T. Kreilos, T. M. Schneider, and S. M. Rubinstein, *Phys. Rev. Lett.* **119**, 224101 (2017).
- [12] A. Košmrlj and D. R. Nelson, *Phys. Rev. X* **7**, 011002 (2017).
- [13] J. W. Hutchinson, *J. Appl. Mech.* **34**, 49 (1967).
- [14] W. T. Koiter, *Proc. Kon. Nederl. Akad. Wet. Amsterdam B* **72**, 40 (1969).
- [15] A. Lee, F. López Jiménez, J. Marthelot, J. W. Hutchinson, and P. M. Reis, *J. Appl. Mech.* **83**, 111005 (2016).
- [16] J. Paulose, G. A. Vliegenthart, G. Gompper, and D. R. Nelson, *Proc. Natl. Acad. Sci. USA* **109**, 19551 (2012).
- [17] S. Knoche and J. Kierfeld, *Soft Matter* **10**, 8358 (2014).
- [18] A. Pogorelov, *Bendings of Surfaces and Stability of Shells*, *Translations of Mathematical Monographs Vol. 72* (American Mathematical Society, Providence, RI, 1988).
- [19] M. Gomez, D. E. Moulton, and D. Vella, *Proc. Royal Soc. A* **472**, 20150732 (2016).
- [20] A. Y. Evkin, *J. Appl. Math. Mech.* **53**, 92 (1989).
- [21] A. Evkin, M. Kolesnikov, and D. A. Prikazchikov, *Math. Mech. Solids* **22**, 1425 (2016).
- [22] W. Meier, *Chem. Soc. Rev.* **29**, 295 (2000).
- [23] H. N. Yow and A. F. Routh, *Soft Matter* **2**, 940 (2006).
- [24] M. P. Neubauer, M. Poehlmann, and A. Fery, *Adv. Colloid Interface Sci.* **207**, 65 (2014).
- [25] O. Seok Kwon, J. Jang, and J. Bae, *Curr. Org. Chem.* **17**, 3 (2013).
- [26] D. Vella, A. Ajdari, A. Vaziri, and A. Boudaoud, *Phys. Rev. Lett.* **109**, 144302 (2012).
- [27] E. Evans and R. Skalak, *Mechanics and Thermodynamics of Biomembranes* (CRC Press, 1980).
- [28] A. Iglic, *J. Biomech.* **30**, 35 (1997).
- [29] G. Lim H. W., M. Wortis, and R. Mukhopadhyay, *Proc. Natl. Acad. Sci. USA* **99**, 16766 (2002).
- [30] G. Lim H. W., M. Wortis, and R. Mukhopadhyay, in *Soft Matter, Vol. 4: Lipid Bilayers and Red Blood Cells*, edited by G. Gompper and M. Schick (Wiley-VCH, Weinheim, 2008) Chap. 2, p. 83.
- [31] J. Lidmar, L. Mirny, and D. R. Nelson, *Phys. Rev. E* **68**, 051910 (2003).
- [32] J. P. Michel, I. L. Ivanovska, M. M. Gibbons, W. S. Klug, C. M. Knobler, G. J. L. Wuite, and C. F. Schmidt, *Proc. Natl. Acad. Sci. USA* **103**, 6184 (2006).
- [33] U. Seifert, *Adv. Phys.* **46**, 13 (1997).
- [34] D. J. Bukman, J. H. Yao, and M. Wortis, *Phys. Rev. E* **54**, 5463 (1996).
- [35] F. Hochmuth, J. Shao, J. Dai, and M. Sheetz, *Biophys. J.* **70**, 358 (1996).
- [36] L. Mesarec, W. Gózdź, S. Kralj, M. Fošnaric, S. Penic, V. Kralj-Iglic, and A. Iglic, *Eur. Biophys. J.* **46**, 705 (2017).
- [37] A. Mietke, O. Otto, S. Girardo, P. Rosendahl, A. Taubenberg, S. Golfier, E. Ulbricht, S. Aland, J. Guck, and E. Fischer-Friedrich, *Biophys. J.* **109**, 2023 (2015).
- [38] A. A. Boulbitch, *Phys. Rev. E* **57**, 2123 (1998).
- [39] G. Salbreux and F. Jülicher, *Phys. Rev. E* **96**, 032404 (2017).
- [40] L. D. Landau and J. M. Lifshitz, *Theory of Elasticity*, Vol. 7 (Pergamon, New York, 1970).
- [41] A. Libai and J. G. Simmonds, *The Nonlinear Theory of Elastic Shells* (Cambridge University Press, Cambridge, UK, 1998).
- [42] S. Timoshenko and J. Gere, *Theory of Elastic Stability* (Tata McGraw-Hill Education, New York, 1961).
- [43] C. Quilliet, *Eur. Phys. J. E* **35**, 48 (2012).
- [44] S. Knoche and J. Kierfeld, *EPL* **106**, 24004 (2014).
- [45] S. Knoche and J. Kierfeld, *Eur. Phys. J. E* **37**, 62 (2014).
- [46] E. Ventsel and T. Krauthammer, *Thin Plates and Shells* (CRC Press, Boca Raton, FL, 2001).
- [47] S. Knoche, *Instabilities and shape analyses of elastic shells* (Ph.D. thesis, Technische Universität Dortmund, Dortmund, Germany, 2014).
- [48] T. V. Karman and H.-S. Tsien, *J. Aeronaut. Sci.* **7**, 43 (1939).
- [49] M. Carin, D. Barthès-Biesel, F. Edwards-Lévy, C. Postel, and D. C. Andrei, *Biotechnol. Bioeng.* **82**, 207 (2003).
- [50] A. Fery and R. Weinkamer, *Polymer* **48**, 7221 (2007).
- [51] A. Fery, F. Dubreuil, and H. Möhwald, *New J. Phys.* **6**, 18 (2004).
- [52] D. Vella, A. Ajdari, A. Vaziri, and A. Boudaoud, *J. R. Soc. Interface* **9**, 448 (2012).
- [53] J. Hegemann, S. Knoche, S. Egger, M. Kott, S. Demand, A. Unverfehrt, H. Rehage, and J. Kierfeld, *J. Colloid Interface Sci.* **513**, 549 (2018).
- [54] E. Reissner, *J. Math. Phys.* **25**, 279 (1946).
- [55] C. Wischniewski, E. Zwar, H. Rehage, and J. Kierfeld, *Langmuir* **34**, 13534 (2018).
- [56] These equations are exactly identical to the leading-order Eqs. (4.8) and (4.9) from Ref. [19] with $2p_0 = F_0/2\pi$.
- [57] This equation is exactly identical to the second-order Eq. (6.3) from Ref. [19] with $2p_1 = F_2/2\pi$.
- [58] A. Y. Evkin, *Int. J. Solids Struct.* **42**, 1173 (2005).
- [59] J. Thompson, *Proc. R. Neth. Acad. Sci.* **67B**, 295 (1964).
- [60] A. Y. Evkin and A. L. Kalamkarov, *Int. J. Solids Struct.* **38**, 8975 (2001).
- [61] N.-C. Huang, *J. Appl. Mech.* **31**, 447 (1964).
- [62] M. Gomez, D. E. Moulton, and D. Vella, *Nat. Phys.* **13**, 142 (2017).
- [63] J. W. Hutchinson, *Proc. Royal Soc. London, Ser. A* **472**, 20160577 (2016).
- [64] M. Pezzulla, N. Stoop, M. P. Steranka, A. J. Bade, and D. P. Holmes, *Phys. Rev. Lett.* **120**, 048002 (2018).
- [65] M. Buenemann and P. Lenz, *Phys. Rev. E* **78**, 051924 (2008).